

**NUMERICAL SIMULATIONS OF THE ISLAND-INDUCED CIRCULATIONS
OVER THE ISLAND OF HAWAII DURING HaRP**

Yang Yang and Yi-Leng Chen*

**Department of Meteorology
SOEST
University of Hawaii at Manoa
Honolulu, HI 96822**

And

Francis M. Fujioka

**Forest Fire Laboratory
US Department of Agriculture
Riverside, CA 92507**

Revised on May 26, 2005

Submitted to Monthly Weather Review

* Corresponding author address: Prof. Yi-Leng Chen, Department of Meteorology, University of Hawaii, Honolulu, HI 96822; email: yileng@hawaii.edu

Abstract

The MM5/LSM is used to simulate the diurnal island-scale circulations over the island of Hawaii during the Hawaiian Rainband Project (HaRP, 11 July – 24 August 1990). The model is initialized with the NCEP/NCAR reanalysis data.

The diurnal variations of the land-sea thermal contrast at the land surface and the planetary boundary layer at Hilo are well simulated. The main discrepancy occurs on the lee-side areas of mountains or ridges below the trade-wind inversion (2 km), where the simulated afternoon land-sea thermal contrast at the surface is 1–3° C lower than observed mainly due to the misrepresentation of lava rocks by the bare ground category in the USGS data and stronger than observed simulated sea breezes bringing in relatively cool maritime air.

The flow deceleration and splitting of the incoming trade-wind flow and the evolution of the diurnal circulation cells on the windward side, the thermally driven diurnal winds, and the wake circulations on the lee side are well simulated. The simulated diurnal variations in rainfall are also in good agreement with observations. However, the simulated winds in areas well exposed to the trade-wind flow are weaker (1–3 m s⁻¹) than observed mainly due to the underestimation of trade-wind flow in the NCEP/NCAR reanalysis. The simulated rainfall over windward lowlands at night is underestimated and the maximum rainfall axis shifts further toward the coast as compared with observations, due to an underestimation of orographic lifting aloft and a relatively large horizontal extent of the simulated katabatic flow because of the weaker than observed trade-wind flow in the initial conditions.

In the afternoon hours on the windward side, the strongest winds (anabatic/sea-breeze and trade-wind flow) are simulated in low levels over land in response to the surface heating, with a westerly wind deviation beneath the mean trade-wind inversion (2 km) and sinking motion over the adjacent oceans. The simulated low-level flow deceleration of the incoming trade-wind flow is most significant in the early morning as a combination of island blocking and nocturnal cooling over land. At that time, the simulated upward motion representing the rising branch of the thermally direct circulation extends more than 40 km offshore.

Sensitivity tests show that with better surface conditions in the model coupled with OSU-LSM, the simulated thermal forcing over land is improved. The improvements in simulated ground temperature, land-sea thermal contrast at the land surface, and mixing ratio lead to better simulation of the strength of land/sea breezes over the island.

1. Introduction

The island of Hawaii, roughly 140 km in diameter, is the largest island of the Hawaiian Island chain. The topography is dominated by two volcanic mountains, Mauna Loa and Mauna Kea, both of which exceed 4,100 m (Fig. 1), and extend well above the typical height of the trade-wind inversion (2 km). In regions of weak winds because of island blocking (Smolarkiewicz et al. 1988), the thermally driven daytime upslope/sea-breeze flow and nighttime downslope/land-breeze flow (Schroeder et al. 1977; Feng and Chen 1998 and others) become significant (Chen and Nash 1994; Feng and Chen 2001). Thermally driven diurnal flows may contribute to rainfall by reinforcing orographic lifting, generating areas of low-level convergence when interacting with the prevailing trade winds (Leopold, 1949; Giambelluca et al. 1986, Schroeder 1981; Feng and Chen 1998; Wang and Chen 1998; Carbone et al. 1998; and others), or producing orographic lifting in areas not exposed to trade winds (Yang and Chen 2003).

High-resolution numerical modeling over the Hawaiian Islands is a significant research challenge. With the presence of steep terrain, heterogeneous soil properties, and vegetation cover, the Hawaiian islands have large spatial variations in local weather ranging from humid tropical conditions on the windward side to semi-arid desert on the lee side. In the past, studies of airflow and cloud development over the island of Hawaii using high-resolution models (Nickerson 1979; Smolarkiewicz et al. 1988; Rasmussen et al. 1989; Rasmussen and Smolarkiewicz 1993; and others) stressed the effects of island blocking. With crude treatments of surface conditions and land surface processes, the island-scale circulations throughout the diurnal cycle (Chen and Nash 1994) were not simulated in sufficient detail.

Chen and Feng (2001) simulated the island-scale airflow and cloud distributions over the island of Hawaii using the fifth generation of the Penn State-National Center for Atmospheric Research (NCAR) Mesoscale Model (MM5) version 1, without considering the diurnal heating cycle. They found that in addition to the Froude number ($Fr = U/Nh$, where U is the upstream wind speed, N is the Brunt-Väisälä frequency, and h is the height of the barrier) (Smolarkiewicz et al. 1988), the simulated island airflow and cloud distributions are sensitive to trade-wind inversion height, net diabatic heating associated with clouds and precipitation and rain evaporative cooling. Feng and Chen (2001) used the same model to successfully simulate the nocturnal flow regime on the windward side. In their work, the land surface is specified as tropical rain forest over the entire island.

From data collected at four major airport sites on Oahu, Zhang et al. (2005a) show that the diurnal variations in the surface parameters over Oahu under summer trade-wind conditions are better simulated by the high-resolution (1.5 km) Mesoscale Spectral Model (MSM) (Juang 2000) coupled with an advanced land surface model (LSM) with improved treatment of the surface conditions as compared with the 10-km operational Regional Spectral Model (Wang et al. 1998). Zhang et al. (2005b) also applied the coupled MSM/LSM with a 3-km resolution to successfully simulate the sea-breeze circulations for a six day period over northwest Hawaii reported by Schroeder (1981), a small area of the island of Hawaii covered mainly by lava rocks.

The simple land surface model of MM5 is conceptually a ground heat budget model, which is capable of predicating soil temperature on five layers but keeping the soil moisture fixed throughout the simulation (Zhang and Anthes 1982). The soil moisture is specified as a function of land use. Recently, the Oregon State University (OSU) land

surface model (LSM) was incorporated into MM5 version 3 (Chen and Dudhia 2001). The OSU-LSM is capable of predicting soil moistures and temperatures on four layers (10, 40, 100 and 200 cm deep). Nevertheless, the land use, soil type, and vegetation fraction over the island of Hawaii generated by the TERRAIN program of MM5 are problematic. For example, there is only one main vegetation type, mixed forest, and three soil types, sandy loam, loam and clay loam. Furthermore, for the month of June, the vegetation fraction is less than 30% for the entire island with a maximum about 28% on the semi-arid leeward area of the Kilauea volcanoes covered by lava rocks. In this study, the MM5/LSM is employed to simulate the island circulations over the island of Hawaii throughout the diurnal cycle using the 30" resolution (1 km) vegetation type, soil type, and vegetation fraction compiled by Zhang et al. (2005a) from the US Geological Survey (USGS) Land Use Land Cover level II data for Hawaii (DOI USGS 1986; Anderson et al. 1976) and the soil survey of the island of Hawaii (Sato et al. 1973).

We performed daily simulations for the entire 45-day period during HaRP with prescribed high-resolution surface properties. One of the advantages of performing case studies for a considerable period of time over theoretical studies is that the model performance can be evaluated with observations. The dense observations from 50 portable automated mesonet (PAM) stations (Fig. 1), Hilo soundings and NCAR Electra aircraft flight-level data collected during HaRP were used to validate the MM5/LSM hourly model results. From PAM data alone, for each surface variable, there are approximately 50,000 ($50 \times 24 \times 45$) data pairs used for simulation vs. observation comparisons. We will investigate to what extent the complete diurnal cycle of island

circulations and weather over the entire island can be simulated by the MM5/LSM with better representation of surface conditions.

In this study, sensitivity tests of planetary boundary layer (PBL) schemes, the simple land surface model of MM5, and OSU-LSM with and without improved surface conditions are also performed. We will show that more realistic thermally driven diurnal island airflows and diurnal evolution of PBL can be simulated by linking MM5 with the OSU-LSM with a better treatment of surface conditions. We will show that the strength of the land/sea breeze circulations over the island and their effects on the airflow over the adjacent water are better simulated by the coupled MM5/LSM with more realistic surface conditions. The model results will also be used to diagnose the diurnal circulation cells on the windward side for both the daytime and nighttime regimes for the first time.

2. Model description and initialization

The MM5 (Dudhia, 1993) is a nonhydrostatic, three-dimensional primitive equation model employing the terrain-following sigma coordinate. In this study, there are 36 sigma levels¹ from the surface to the 100-hPa level with 13 levels below sigma = 0.9. Four domains with two-way nesting were used with horizontal resolutions of 81 km, 27 km, 9 km and 3 km, respectively (Fig. 2). With a 3-km resolution, 41 of the 50 PAM stations have elevation errors smaller than 50 m in the model terrain (not shown). Many of them have elevation errors only a few meters and only 3 stations (stations 18, 35, and 38) have elevation errors larger than 100 m. The largest errors in the model terrain occur near the summits of Mauna Loa, Mauna Kea, and the Kohala Mountains with errors of 140 m, 266

¹ The full sigma levels are: 1., 0.999, 0.998, 0.996, 0.994, 0.992, 0.990, 0.988, 0.985, 0.980, 0.97, 0.945, 0.91, 0.865, 0.82, 0.79, 0.76, 0.73, 0.7, 0.67, 0.64, 0.61, 0.58, 0.55, 0.52, 0.475, 0.425, 0.375, 0.325, 0.275, 0.225, 0.175, 0.125, 0.075, 0.025, 0.0

m, and 100 m, respectively. It is apparent that the 3-km resolution used in the finest nested domain is adequate in resolving the terrain in the vicinity of most HaRP stations.

We used the Grell cumulus parameterization, grid-scale warm rain process (Hsie et al. 1984), a cloud-radiation scheme (Dudhia and Moncrieff 1989), and Hong and Pan's (1996) boundary layer scheme. Because trade-wind cumuli moving toward the island to produce rain showers under summer trade-wind conditions are small and not well resolved by a 3-km grid, the Grell cumulus parameterization is also used in the 3-km resolution domain.

In this study, the MM5 was initialized by the NCEP/NCAR reanalysis data. Because of the low resolution of the data set ($2.5^{\circ} \times 2.5^{\circ}$), the soil moisture cannot be generated from the reanalysis data for the Hawaiian island chain. Furthermore, the soil moisture depends on the local weather conditions in the past. To solve this problem, MM5/LSM was run for two months prior to the HaRP period with the initial soil moisture specified according to the soil type. During this two-month period, the soil moistures and soil temperatures are updated daily from the 24-h forecast of the previous day. The soil moistures (Fig. 3) and soil temperatures after two-month simulations are used to initialize LSM for our HaRP simulations. Starting from 10 July, the simulation for each day during HaRP was initialized at 1200 UTC using the 24-h forecasts of the soil moistures and soil temperatures of the previous day and run for 36 hours. The results from the 12th hour and the 36th hour for each simulation were used to represent the simulated diurnal cycle of the following day. Using Clark's model to simulate the airflow over the island of Hawaii, Smolarkiewicz et al. (1988) show that the energy spectrum reaches a quasi-steady state after 3-h integration when the boundary layer airflow has relaxed to a stable solution. For

the numerical studies using MM5 by Chen and Feng (2001) for the island of Hawaii, and by Yeh and Chen (2003) for the island of Taiwan, the PBL “spin-up” time is also on the order of 3-h simulation time. Therefore, a 12-h period is long enough to spin up the PBL in the model.

3. Simulated island-scale airflow and weather

3.1 Simulated mean surface winds

3.1.1 Over the island

The 45-day averaged diurnal variations of surface winds from 50 PAM observations during HaRP (Fig. 4a) will be compared with model simulations (Fig. 4b). The simulated winds at grid points of the finest domain (3 km resolution) were interpolated to the locations of PAM stations.

The observed weak winds in the Hilo Bay area and on the windward slopes as well as the splitting airflow along the windward coast as a result of island blocking are well simulated (Fig. 4). In addition to the northern and southern parts of the island, strong winds are also simulated in the Humu'ula Saddle between Mauna Loa and Mauna Kea and in the Waimea Saddle (Fig. 4b). In the Kona area behind Mauna Loa and Mauna Kea, the trade winds are completely blocked by the mountains with relatively calm winds. These features are in good agreement with observations (Fig. 4a).

The main discrepancies of the u -wind component between the simulated and observed mean winds occur in regions well exposed to the easterly trade-wind flow, including the northern (stations 32, 34 and 35) and southern parts (stations 1, 2, 46 and 48) of the island, in the Humu'ula Saddle (stations 19 and 20) between Mauna Loa and Mauna Kea mountains, and downstream of the Waimea Saddle (stations 36, 37 and 28)

(Fig. 5a). In these regions, the simulated easterly winds are weaker than observed with the largest differences reaching $2 - 3 \text{ m s}^{-1}$ over the northern and southern parts of the island (stations 1, 46 and 35) (Fig. 5a).

Over the Hawaiian Islands there are only two rawinsonde sites. One is at Lihue on Kauai and the other is at Hilo (Fig. 6). The low-level winds from Hilo soundings are greatly affected by island blocking with weak speeds than those over the open ocean. Due to the use of Hilo soundings, there is an area with weak mean trade-wind speed (outlined by contour line of 6.5 m s^{-1}) extending about 400 km upstream of Hilo in the NCEP/NCAR reanalysis (Fig. 6). The open ocean trade-wind speed upstream of Hilo is underestimated. Figure 7 shows the mean wind and temperature profiles of 22 early morning soundings constructed from the aircraft flight-level data over the open ocean upstream of Hilo. For each day with an early morning aircraft sounding, a linear interpolation scheme is used to interpolate the initial data at 0200 HST used by the model to the height of each aircraft data point. The mean winds from the NCEP/NCAR reanalysis at 0200 HST are $1.0 - 3 \text{ m s}^{-1}$ weaker than the aircraft observations below 2.4 km with relatively large errors at low levels (Fig. 7). The weaker than observed winds simulated in the areas well exposed to the trade-wind flow are mainly caused by errors introduced by the NCEP/NCAR reanalysis used in the initial conditions.

Averaging over the entire diurnal cycle, the large differences between the simulated and observed mean v in the Kona area (stations 40, 41, 42, 43 and 45) in the pure dynamic run by Chen and Feng (2001) are largely corrected in this study. The main discrepancies ($1-1.5 \text{ m s}^{-1}$) occur over the northern area (stations 21, 29, 31 and 32), southeastern corner (station 1 and 46) of the island and downstream of the Waimea

Saddle (stations 37, 38 and 28) (Fig. 5b). Relatively large differences (2 m s^{-1}) between the simulated and observed mean v also occur at station 3 and 5 in the southeastern area of the island near the Kilauea volcanoes. As noted by Chen and Nash (1994), wind observations at station 5 are questionable because this PAM station was not well exposed to the environmental winds.

3.1.2 Wake circulations

The airflow over the ocean on the lee side of the island of Hawaii was first reported from ship observations over a 15-yr period (Patzert 1969) (Fig. 8a). The first aircraft probing of the wake was made in the summer of 1980 (Nickerson and Dias 1981) with the first direct evidence for the existence of lee vortices. From HaRP aircraft flight-level data, Smith and Grubisic (1993) showed that the Hawaii's wake consists of two quasi-steady eddies that give rise to a wide region of reversed flow along the wake axis. The leeside eddies were also simulated by Nickerson (1979), Smolarkiewicz et al. (1988), and Ueyoshi (1990).

From the mean simulated surface winds of the 3-km resolution domain (Fig. 8b), the horizontal wake zone, the two vortices and the westerly reversed flow are well simulated and agree well with the mean 15-yr ship observations (Fig. 8a). On the northwestern leeside area of the island of Hawaii, the westerly flow over the ocean in the small wake (Smith and Grubisic, 1993) is also well simulated. However, the simulated large wake zone and the return flow shift southward as compared with observations (Fig. 8a).

3.2 Simulated surface thermodynamic fields

Chen and Wang (1994) show that the diurnal ranges in surface air temperature vary considerably over the island of Hawaii related to land surface properties, orography,

airflow, and distributions of cloud and rain. They also show that the diurnal variations of the surface airflow over the island are closely related to the temperature fields. Since our interest is on the land-sea thermal contrast, similar to Chen and Wang (1994), the mean sounding over the open ocean constructed from 22-day aircraft flight-level data during HaRP will be used as the reference. The simulated surface temperature deviation at each PAM station is calculated by subtracting the observed air temperature over the open ocean at the same level from the simulated surface air temperature. For the observed temperature deviation at each PAM station, the actual station elevation is used as the reference level for the calculation of temperature deviation. By using temperature deviations, the possible temperature biases introduced by elevation errors in the model terrain will be eliminated even though these errors are rather small in most cases.

At 1400 HST, as found by Chen and Wang (1994), the observed mean temperature deviations from the upstream aircraft flight-level data at the same level are in the range of $1.5\text{--}3^{\circ}\text{C}$ on the windward side with the smallest values along the windward coast, whereas in the lee-side areas, the deviations are larger ($3\text{--}6^{\circ}\text{C}$) with the largest values in the semiarid regions: over the lee side of the Kilauea volcanoes, southwestern corner, downstream of the Waimea Saddle and the summits of Mauna Kea and Mauna Loa (Fig. 9a). These features are well simulated in the model (Fig. 9b). In addition, the model also simulates large deviations ($> 5^{\circ}\text{C}$) in the data-void semiarid region downstream of the Humu'ula Saddle.

During the daytime, the largest model bias occurs on the lee side of the Kilauea volcanoes (station 3), southwestern corner (stations 1 and 46) and the Waikoloa coast downstream of the Waimea Saddle (stations 36 and 37) where the simulated surface

temperature deviations are 1-3° C lower than observed (Figs. 9a, b). The dominant land use category in these semi-arid regions is lava rock, whereas in the USGS data, it is erroneously specified as bare ground. The MM5/LSM used in this study does not have lava rock as one of the land use categories. The black lava rocks contain little soil moisture with low albedo, low heat capacity, and low thermal conductivity. The discrepancies of the land surface properties in these areas would introduce a cold bias in the simulated surface air temperature during the daytime in the model (Zhang et al. 2005b). In addition, these regions are well exposed to the descending trade-wind flow in the lee (Fig. 4a). As will be shown later, with a weaker opposing trade-wind flow in the model (Fig. 4b), the simulated sea-breeze circulations in these regions are more pronounced than the observed and bring in cooler air from the adjacent oceans.

In the early morning, the largest negative temperature deviations ($< -4^{\circ}\text{C}$) are over high mountain areas above the trade-wind inversion (2 km) and in the Hilo coastal areas. The smallest negative temperature deviations ($-1 - -2^{\circ}\text{C}$) are in the lee-side coastal areas. The overall temperature pattern and the magnitudes of simulated negative temperature deviations are in good agreement with observations (Figs. 9c, d).

To assess how well the thermal contrast is simulated during the diurnal cycle from day to day during HaRP, the root mean square errors (RMSE) of the surface air temperature deviation at 50 PAM stations were calculated (Fig. 10). Relatively large ($2-4^{\circ}\text{C}$) RMSE occur on the northwestern and southwestern lee-side areas of the island, and the lee side of the Kilauea volcanoes in the afternoon hours (Fig. 10a). During the nighttime, the RMSE are about 1°C at most windward side and lee-side stations (Fig. 10b). It is apparent that the land-sea thermal contrast at the land surface during the

diurnal cycle is well simulated by MM5/LSM except in these lee-side areas in the afternoon hours.

For a pure dynamic run without considering the diurnal cycle (Chen and Feng 2001), the predicted surface relative humidity on the Kona side (stations 39, 40, 41, 42, 43, 45, 46 and 47) is 15-30% lower than the observed mean relative humidity at these sites. Chen and Feng (2001) suggest that the discrepancies are mainly related to the development of the upslope/onshore flow during the daytime on the Kona side that brings in maritime air there (Chen and Nash 1994; Chen and Wang 1995). With simulations of the full diurnal cycle, this problem is corrected in this study (Fig. 11).

3.3 Diurnal variations of the simulated winds

3.3.1 Surface winds over the island

With successful simulations of the land-sea thermal contrast over the diurnal heating cycle, we will validate both the simulated daytime and nighttime flow regimes over the entire island using the PAM observations.

The simulated surface airflow at 1400 HST (Figs. 12a, b) reproduces the observed combined anabatic/trade-wind flow on the windward side, a splitting airflow with strong winds over the northern and southern tips, strong winds over the Waimea Saddle and the Humu'ulu Saddle, and the sea breezes along the Kona coast. At 0200 HST, the katabatic/offshore flow is well simulated over most areas of the island except in regions with strong winds: the northern and southern tips, the Waimea Saddle, and the Humu'ulu Saddle (Figs. 12c, d). These results are in agreement with observations.

For stations on the windward lowlands west of Hilo with weak mean winds because of island blocking, the time of the winds turning from the downslope (upslope) flow to

the upslope (downslope) flow during the morning (evening) transition agrees with observations reasonably well (Fig. 13).

Because of a weaker incoming trade-wind flow in the model, the main discrepancies occur in regions well exposed to the trade-wind flow where the simulated surface winds are $1\text{--}3\text{ m s}^{-1}$ weaker than observed. In addition, at Cape Kumukahi over the eastern end of the island, the simulated katabatic flow is $1\text{--}2\text{ m s}^{-1}$ stronger than observed (Figs. 12c, d). On the average, the offshore flow does not appear at Cape Kumukahi until 0400 HST (Chen and Nash 1994); however, the simulated surface flow exhibits offshore flow there at 0200 HST. Furthermore, for station 3 on the lee side of the Kilauea volcanoes and station 46 on the southwestern corner, the observed winds at 1400 HST are relatively strong ($> 5\text{ m s}^{-1}$) with a northerly wind component (Fig. 12a). In contrast, with a weaker upstream trade-wind flow in the model, the sea breezes are simulated in the model at both stations with a notable southerly wind component there (Fig. 12b).

3.3.2 Low-level airflow offshore of Hilo

In this section, we will show that the effects of the diurnal heating cycle on the low-level airflow offshore of Hilo are well simulated. During HaRP, the airflow immediately upstream of Hilo was sampled by the NCAR Electra with a box flight pattern at 150 m above the sea level. Most of the box-pattern flight missions were conducted in the late afternoons (or early evenings) or early mornings. The model output is in 1-h intervals. A linear interpolation scheme is used to interpolate the model output data to the flight observation points in both space and time.

In the late afternoon of 1 August (Fig. 14a), the easterly and southeasterly winds on the northwestern corner of the flight box and the northeasterly winds on the southwestern

corner of the flight box are well simulated (Fig. 14b). Along the northwest-southeast flight leg immediately upstream of the Hilo coast, the simulated winds are weaker than farther upstream as a result of island blocking, in good agreement with observations.

There are some discrepancies between the simulated and observed winds (Fig. 14a, b). Along the center flight leg of the flight box, the simulated wind speed is about 2-4 m s⁻¹ smaller than observed. Part of the differences could be attributed to the weak trade-wind flow in the model. In addition, the uncertainties in the aircraft wind measurements could be another factor. The intersection of the northwest-southeast flight leg immediately upstream of Hilo and the central flight leg in the flight box was visited twice by the aircraft about half an hour apart (Fig. 14a). The observed wind speed differences between the two visits are as large as 4 m s⁻¹.

In the early morning of 2 August (Figs. 14c, d), both the observations and model results show that the flow deceleration along the central flight leg is more significant than the late afternoon flight. The flow splitting with southeasterly flow in the northwestern corner and northeasterly flow in the southwestern corner of the flight box are also more pronounced than in the late afternoon. In the central portion of the northwest-southeast flight leg immediately upstream of Hilo, the westerly land breezes are simulated.

3.4 Simulated diurnal variations of the planetary boundary layer at Hilo

In this section, we compare the simulated diurnal variations of winds and thermodynamic structure in the boundary layer with observations. First of all, a comparison is made between the vertical profiles of mean winds at 0200 HST and 1400 HST during HaRP from Hilo rawinsonde data and the results from MM5 simulations (Fig. 15).

At 0200 HST, the simulated depth of the offshore/katabatic flow is 500 m, consistent with observations (Fig. 15). At 1400 HST, relatively strong winds are simulated at low levels as a result of the development of the combined anabatic/trade-wind flow. Substantial day/night differences in winds aloft are also simulated, especially just beneath the mean level of trade-wind inversion (2 km). Stronger easterly winds are simulated there at night with weaker winds during the day. These results are in good agreement with observations (Fig. 15).

During 10 August 1990, rawinsondes were launched every 3 hours at Hilo. The diurnal evolution of potential temperature profiles within the planetary boundary layer with a 3-h interval during 10 August is shown in Figure 16a. This is a low trade-wind inversion day with an inversion height of 1.4 km (Feng and Chen 1998). At 1400 HST, the simulated potential temperature is well mixed below the 950-hPa level (Fig. 16b). The simulated nocturnal inversion forms in the early evening (1800 HST) with the deepest nocturnal inversion (50 hPa) just before sunrise. The simulated nocturnal inversion at Hilo disappears around 1000 HST. These results are in good agreement with observations. However, the simulated potential temperature profile above the surface layer has a cold bias on the order of 1 K. The simulated trade-wind inversion (875 hPa) (Fig. 16b) are weaker with a smaller vertical gradient of potential temperature than observed (Fig. 16a). Note that the trade-wind inversion is poorly resolved in the initial conditions because of a coarse vertical resolution in the NCEP/NCAR reanalysis. Since the trade-wind inversion is caused by large-scale subsidence associated with the semi-permanent subtropical high, the time scale for the simulated trade-wind inversion to reach the observed strength may be more than one day.

4. Sensitivity tests

In this section, five sensitivity tests with different boundary layer schemes, land surface conditions, and land surface models are conducted (Table 1). A simple soil model, Blackadar boundary layer scheme (Zhang and Anthes 1982) and MM5 land surface data are used in TEST1. TEST2 is the same as TEST1 except the MRF boundary layer scheme (Hong and Pan 1996) is used. For TEST 3, OSU-LSM, MRF boundary layer scheme and MM5 land surface data are used. TEST 4 is the same as TEST3 except using the surface data compiled by Zhang et al. (2005a). CTL uses the same surface data as TEST4 except that the soil moisture and soil temperature were updated daily after a two-month spin-up period of soil parameters. TEST 5 is the same as CTL except the eta boundary layer scheme (Janjic 1994) is used. All the sensitivity tests are initialized at 0200 HST, 9 August with a 36-hour simulation. The simulated data from 12th to 36th hour are used for analysis. The temperature deviations and mixing ratio in TEST1 for Tables 2 and 3 are from the lowest model level about 5 m above the surface. For all other runs, the 2-m temperature deviations and mixing ratio are used.

4.1 Surface air temperature and mixing ratio

At 1400 HST, all the simulations show a cold bias (simulation – observation, Table 2). Note that in the planetary boundary layer, MM5 results already have a cold bias (1 K, Figs. 16a, and b). In other words, part of the cold bias is not related to the land surface processes. TEST1 has the largest cold bias. Replacing the Blackadar boundary scheme with the MRF scheme results in improvements in the simulations of afternoon surface air temperature deviations (TEST1 vs. TEST2). Note that replacing the simple land surface model with OSU-LSM alone does not result in significant improvements in the simulated

surface air temperature deviations and moistures (TEST2 vs. TEST3). Additional improvements in the simulated surface thermodynamic fields are achieved only by using OSU-LSM together with better representations of surface properties, and better initial conditions in soil moistures and temperatures (TEST3 vs. CTL).

At 0500 HST (Table 3), all the simulations show a warm bias except TEST5. The differences in error statistics between TEST1 and CTL are less significant at 0500 HST as compared to the daytime error statistics. It is apparent that the nocturnal flow regime is less affected by the boundary layer model, land surface model and the land-surface properties used as compared with the daytime flow regime.

At both 1400 HST and 0500 HST, the RMSE and the mean absolute errors of the surface air temperature deviations are the smallest for CTL. For the mixing ratio, the RMSE and mean absolute errors are also the smallest for CTL. It is apparent that with OSU-LSM and better treatment of initial lower boundary conditions at the surface, the simulated surface air temperature deviations and mixing ratio are improved.

4.2 Ground temperature in the afternoon

Observations show that the soil temperature at 6 mm at the summit of Mauna Kea, June 1980 exceeds 32° C in the afternoon with a diurnal range of 35° C (Schroeder 1993). Since surface fluxes during the day are related to the ground temperature and were not measured during HaRP, simulated ground temperatures at 1400 HST are examined.

For TEST1, the simulated ground temperature in the afternoon at the summits of Mauna Kea and Mauna Loa is only 12° C (Fig. 17a), more than 20° C lower than observed. The simulated ground temperature is improved in TEST3 with MRF boundary layer scheme and OSU-LSM (Fig. 17b), but is still 10° C lower than observations. With

improved land surface conditions in CTL (Fig. 17c), the simulated ground temperature there (32° C) is closer to observations. On the leeward side of Waimea Saddle, the maximum ground temperatures in the coastal region are 38° C for CTL, 34° C for TEST 3, 30° C for TEST 1. The simulated ground temperature there and other semi-arid regions would be higher than CTL with a lower cold bias in the surface air temperature if correct surface parameters for lava rocks are specified (Zhang et al. 2005b).

During HaRP, three PAM stations (15, 16 and 17, Fig. 1) have ground temperature observations (Table 4). Station 17 in Humu'ula Saddle is mainly covered by lava rock. The land use category at station 17 is bare ground in CTL and TEST3, but mixed forest in TEST1. In addition, the vegetation cover is 0 for CTL and TEST3, but 25% for TEST1. At 1400 HST 10 August 1990, the observed ground temperature is 36.6 ° C, whereas simulated ground temperature is 32° C, 24° C and 16° C for the CTL, TEST2 and TEST1, respectively. All three simulations underestimate the ground temperature there with the smallest error in CTL. The observed ground temperatures at 1400 HST at stations 15 and 16 are 30.9° C and 22.1° C, respectively. The simulated ground temperatures at these two stations are 25° C and 21° C for the CTL, 25° C and 20° C for TEST3, and 22° C and 18° C for TEST1, respectively. The differences in the simulated ground temperature at these two sites among TEST1, TEST3 and CTL are smaller than those of station 17. At these two sites, the land use is mixed forest and the soil type is sandy loam for CTL, TEST3 and TEST1. The vegetation cover is 20% at these stations for TEST1 and TEST3 but 80% for CTL.

It is apparent that with improved lower boundary conditions, the coupled MM5/LSM performs better than other runs in terms of simulated surface temperature, moisture and

ground temperature. To assess the impact of improved surface boundary conditions on the strength of thermally driven diurnally circulations, the observed and simulated mean island-scale divergence throughout the diurnal cycle is computed from observed and simulated surface wind data at 21 PAM stations along the coastline, respectively (Fig. 18). The observations show convergence during the daytime and divergence at night due to land/sea breezes. TEST3 underestimates the convergence during the daytime and divergence at night. This problem is largely corrected in CTL. With improved initial and lower boundary conditions at the surface in CTL over TEST3, the performance of the model in simulating the strength of land/sea-breeze circulations is also improved.

5. Evolution of the diurnal circulation cells on the windward side

In the past, the diurnal circulation cells on the windward side were inferred from the surface data and Hilo soundings (Garrett 1980; Chen and Nash 1994). The modeling study of Feng and Chen (2001) and HaRP case studies (Feng and Chen 1998; Li and Chen 1999; Frye and Chen 2001) focused on the nocturnal flow regime. In this section, the simulated nighttime and daytime circulation cells on the windward side will be diagnosed from model results.

The simulated katabatic flow starts around 1900 HST on the windward lowlands west of Hilo (Fig. 13) and extends both upward and toward the coast (Fig. 19a), in agreement with PAM observations (Chen and Nash 1994). The simulated vertical cross section shows a cold pool on the windward lowlands west of Hilo (Fig. 19b). As the night progresses, the cold pool becomes deeper and gradually extends offshore as the cold air on the slope surface moves down the slope (Fig. 20). The maximum rainfall axis shifts toward the coast in the early evening (Figs. 21a and b) as found by Feng and Chen

(1998). The nocturnal rainfall maximum occurs on the windward lowlands and coastal areas (Fig. 21b). These results are in agreement with rainfall distribution from PAM observations (Chen and Feng 1995) (their Fig. 8). However, under a weaker than observed incoming trade-wind flow in the model, the simulated katabatic flow extends farther offshore than observed. In addition, the orographic lifting of trade-wind flow aloft would be weaker. As a result, the convergence zone shifts toward the coast with less simulated rainfall (Figs. 21a and b) as compared with observations (Chen and Feng 1995).

Just before sunrise, the simulated offshore flow extends the farthest off the coast (30 km) with the deepest cold pool (500 m) in the Hilo Bay area (Fig. 22a). The parabolic wind profile (Takahashi 1986) is simulated. The simulated maximum rainfall occurs along the coastal areas (Figs. 21c and d) in agreement with observations (Chen and Feng 1995), as the frequently observed rainbands or trade-wind showers move over the deep offshore flow and dissipate (Wang and Chen 1998). The simulated evolution of the nocturnal regime is consistent with Feng and Chen (2001) who used MM5 version 1 with the Blackadar boundary layer scheme and a simple land surface model.

Because of a shallow nocturnal inversion on the upper slope and a deep cold pool (500 m) on the windward lowlands and coastal region, the turning of downslope/offshore flow to upslope/onshore flow after sunrise as a result of solar heating starts from the upper slopes (Fig. 23a) in agreement with Chen and Nash (1994). At 0800 HST, the simulated winds on the slope surface have turned from downslope to upslope flow with offshore flow on the windward lowlands and coastal area. At this time, the simulated

shallow nocturnal inversion on the slopes disappears and is replaced by a superadiabatic layer (Fig. 23b), whereas the cold pool in the Hilo Bay area is still present.

In the afternoon hours, the strongest winds are simulated in the lower levels over land and over the ocean in response to the surface heating as the combined anabatic/sea-breeze and trade-wind flow moves up the slopes (Fig. 24a). The flow deceleration upstream in lower levels is not significant. The cold pool in the Hilo Bay area disappears in the late morning (Fig. 16b) and is replaced by a superadiabatic surface layer (Fig. 24b). During the daytime, the simulated maximum rainfall occurs on the windward slopes (Figs. 21e and f) due to orographic lifting of the combined anabatic/trade-wind flow (Fig. 24a), in agreement with observations (Chen and Feng 1995).

At night, the deviations of u from the mean state show a westerly wind component on the slope surface extending more than 40 km offshore with a weak easterly wind component aloft (Fig. 25a). The flow deceleration upstream in the early morning is a combination of island blocking (Smolarkiewicz et al. 1988; Carbone et al. 1998; Wang et al. 2000) and thermally driven circulation in response to the diurnal heating cycle (Chen and Nash 1994; Feng and Chen 2001). Rising motion not only occurs at the leading edge along the cold pool, but farther upstream due to significant deceleration of the incoming trade-wind flow (Fig. 25b). Intensification of incoming trade-wind cumuli offshore (Austin et al. 1996) is more significant in the early morning than any other diurnal time periods in response to the rising branch of thermal direct circulation (Fig. 25c) in addition to island blocking. Further intensification of the trade-wind cumuli occurs at the leading edge of the drainage front (Leopold 1949; Garrett 1980; Takahashi 1981; Wang and Chen 1998). The distribution of equivalent potential temperature shows that the trade-wind

inversion is lifted in the coastal areas and offshore in response to the thermally direct secondary circulation (Fig. 25d). Lifting of the trade-wind inversion is also evident above the lower windward slope due to the orographic lifting aloft.

For the afternoon flow regime, the deviations of u shows an easterly wind component in the lowest levels over the slope surface and the coastal waters more than 40 km offshore (Fig. 26a). A westerly wind deviation representing the return branch of the sea-breeze/onshore flow occurs beneath the mean trade-wind inversion (2 km), where the deceleration of incoming trade-wind flow is most significant as the flow encounters the return flow. Another return branch occurs above the trade-wind inversion associated with the upslope flow that penetrates the trade-wind inversion on the upper slopes. The orographic lifting on the windward slopes is enhanced by the combined anabatic/trade-wind flow during the daytime (Fig. 26b) with sinking motion over the adjacent oceans (Fig. 26c). As a result, the convection offshore is suppressed during the daytime (Chen and Feng 1995). Trade-wind cumuli moving toward the island with the trade-wind flow frequently dissipate before reaching the island during the daytime. The equivalent potential temperature distribution (Fig. 26d) shows that the trade-wind inversion is lifted above the windward slopes but is pushed downward over the adjacent ocean.

6. Summary

Initialized with the NCEP/NCAR reanalysis data, the MM5/LSM is used to simulate the diurnal island-scale airflow and weather over the Island of Hawaii with improved initial and boundary conditions at the surface.

The simulated diurnal land-sea thermal contrast at the land surface and the diurnal evolution of planetary boundary layer at Hilo are in good agreement with observations. In

the early morning, the observed large negative temperature deviations ($< -3^{\circ}\text{C}$) over high mountains above the trade-wind inversion (2 km) and in the Hilo coastal areas, and small negative temperature deviations (-1 – -2°C) in the lee-side coastal areas are well simulated in the model. At 1400 HST, relatively large (3 – 6°C) temperature deviations in the lee-side areas with the largest values in the semiarid regions (over the lee side of the Kilauea volcanoes, the southwestern corner, the northwestern leeward, and the summits of Mauna Kea and Mauna Loa) are well simulated.

The simulated land-sea thermal contrast shows a cold bias at the land surface in the afternoon hours, especially in the semiarid regions where the simulated afternoon land-sea thermal contrast is 1 – 3°C lower than observed. In these areas, the misrepresentation of lava rocks by the bare ground category in USGS data would contribute to the errors (Zhang et al. 2005b). In lee-side areas with mountain ridges below the trade-wind inversion, the simulated stronger-than-observed sea breezes also bring relatively cool marine air into these regions. The simulated wind speed in regions well exposed to the trade-wind flow is weaker than observed, with differences of 1 – 3 m s^{-1} , due to the underestimation of the upstream trade-wind strength by the NCEP/NCAR reanalysis.

In the afternoon hours, the strongest winds (anabatic/sea-breeze and trade-wind flow) are simulated in the lower levels in response to the surface heating. A westerly wind deviation representing the return branch of the sea-breeze/onshore flow occurs beneath the mean trade-wind inversion (2 km). The orographic lifting on the windward slopes is enhanced by the combined anabatic/trade-wind flow during the daytime with sinking motion over the adjacent oceans. Another return branch occurs above the trade-wind

inversion associated with the upslope flow that penetrates the trade-wind inversion on the upper slopes

During the evening transition, the simulated katabatic flow starts around 1900 HST on the windward lowlands west of Hilo and extends both upward and toward the coast. Just before sunrise, the simulated offshore flow extends the farthest off the coast with the deepest (500 m) cold pool in the Hilo Bay area. Because of a relatively shallow nocturnal inversion and rapid surface heating on upper slopes, the simulated turning of downslope/offshore flow to upslope/onshore flow after sunrise starts from the upper slopes. These features are in good agreement with observations.

The simulated flow deceleration of the incoming trade-wind flow on the windward side is most significant in the early morning as a combination of island blocking and nocturnal cooling over land. The thermally direct secondary circulation in the early morning is characterized by a parabolic wind profile upstream, descending air immediately above the slope surface, and rising motion offshore with significant flow deceleration before the incoming trade winds encounter the cold pool in the coastal area. The simulated upward motion representing the rising branch of the thermally direct circulation driven by land-sea thermal contrast extends more than 40 km from the coast.

During the daytime, the simulated maximum rainfall occurs on the windward slopes due to orographic lifting. During the evening transition, the simulated maximum rainfall axis shifts toward the coast as the downslope flow develops in the lowlands west of Hilo and gradually extends toward the coast. The simulated nocturnal rainfall maximum occurs on the windward lowlands and coastal areas. In the early morning, the simulated maximum rainfall occurs along the coast. These features are in agreement with the

observations. However, The simulated rainfall over windward lowlands at night is underestimated and the maximum rainfall axis shifts further toward the coast as compared with observations, due to an underestimation of orographic lifting aloft and a relatively large horizontal extent of the simulated katabatic flow because of the weaker than observed trade-wind flow in the initial conditions.

Sensitivity tests show that with better surface conditions in the model coupled with OSU-LSM, the simulated thermal forcing over land is improved. The improvements in simulated ground temperature, land-sea thermal contrast and mixing ratio lead to better simulation of the strength of land/sea breezes over island.

Acknowledgments. The authors wish to thank NCAR MM5 group for the applications of the MM5/LSM, anonymous reviewers for their comments, and D. Henderson for editing the text. This work is supported by the National Science Foundation under Grant ATM-0140387 and the U. S. Department of Agriculture under Cooperative Research Agreement 05-JV-11272165-015. We thank the university of Hawaii and MHPCC (Maui High Performance Computing Center) for their support of this project.

References

- Anderson, J. R., E. E. Hardy, J. T. Roach, and R. E. Witmer, 1976: A Land Use and Land Cover Classification System for Use with Remote Sensor Data. U.S. Geological Survey, Professional Paper 964, p 28, Reston, VA.
- Austin, G. R., R. M. Rauber, H. T. Ochs III, and L. J. Miller, 1996: Trade-wind clouds and Hawaiian rainbands. *Mon. Wea. Rev.*, **124**, 2126-2151.
- Carbone, R. E., J. D. Tuttle, W. A. Cooper, V. Grubisic, and W. C. Lee, 1998: Trade wind rainfall near the windward coast of Hawaii, *Mon. Wea. Rev.*, **126**, 2847-2863.
- Chen, F., and J. Dudhia, 2001: Coupling an advanced land surface-hydrology model with the Penn State-NCAR MM5 modeling system. Part I: Model Implementation and Sensitivity. *Mon. Wea. Rev.*, **129**, 569–585.
- Chen, Y.-L., and J. Feng, 2001: Numerical simulations of airflow and cloud distributions over the windward side of the island of Hawaii. Part I: The effects of trade wind inversion, *Mon. Wea. Rev.*, **129**, 1117-1134.
- _____, and J.-J. Wang, 1995: The effects of precipitation on the surface temperature and airflow over the island of Hawaii. *Mon. Wea. Rev.*, **123**, 681-694.
- _____, and J. Feng, 1995: The influence of inversion height on precipitation and airflow over the Island of Hawaii. *Mon. Wea. Rev.*, **123**, 1660-1676.
- _____, and J.-J. Wang, 1994: Diurnal variations of surface thermodynamic fields on the island of Hawaii. *Mon. Wea. Rev.*, **122**, 2125–2138.
- _____, and A. J. Nash, 1994: Diurnal variations of surface airflow and rainfall frequencies on the island of Hawaii. *Mon. Wea. Rev.*, **122**, 34-56.

- DOI USGS, 1986: Land Use Land Cover Digital Data from 1:250,000 and 1:100,000 - Scale Maps. Data User Guide 4, U.S. Geological Survey, Reston, VA.
- Dudhia, J. 1993: A nonhydrostatic version of the Penn state-NCAR mesoscale model: validation tests and simulation of an Atlantic cyclone and cold front. *Mon. Rea. Rev.*, **121**, 1493-1513.
- _____, and M. W. Moncrieff 1989: A three-dimensional numerical study of an Oklahoma squall line containing right-flank supercells. *J. Atmos. Sci.*, **46**, 3363–3391.
- Feng, J., and Y.-L. Chen, 2001: Numerical simulations of airflow and cloud distributions over the windward side of the island of Hawaii. Part II: Nocturnal flow regime, *Mon. Wea. Rev.*, **129**, 1135-1147.
- _____, and _____, 1998: Evolution of Katabatic flow on the island of Hawaii during 10 August 1990. *Mon. Wea. Rev.*, **126**, 2185-2199.
- Frye, J., and Y.-L. Chen, 2001: Evolution of downslope flow under strong opposing trade winds and frequent trade-wind rainshowers over the island of Hawaii. *Mon. Wea. Rev.*, **129**, 956-977.
- Garrett, A. J., 1980: Orographic cloud over the eastern slopes of Mauna Loa volcano, Hawaii, related to insolation and wind. *Mon. Wea. Rev.*, **108**, 931–941.
- Giambelluca, T. W., M. A. Nullet, and T. A. Schroeder, 1986: Rainfall atlas of Hawaii. Report R76, Department of Land and Natural Resources, State of Hawaii, Honolulu, HI, 267 pp.
- Hong, S.-Y., and H. L. Pan, 1996: Nonlocal boundary layer vertical diffusion in a medium –range forecast model. *Mon. Wea. Rev.*, **124**, 2322-2339.

- Hsie, E.-Y., R. A. Anthes and D. Keyser, 1984: Numerical simulation of frontogenesis in a moist atmosphere. *J. Atmos. Sci.*, **41**, 2581-2594.
- Janjic, Zavisla I., 1994: The step-mountain eta coordinate model: Further development of the convection, viscous sublayer, and turbulent closure schemes. *Mon. Wea. Rev.*, **122**, 927-945.
- Juang, H. – M., 2000: The NCEP mesoscale spectral model: A revised version of the nonhydrostatic regional spectral model. *Mon. Wea. Rev.*, **128**, 2329-2362.
- Leopold, L. B., 1949: The interaction of trade wind and sea breeze, Hawaii. *J. Meteor.*, **8**, 533- 541.
- Li, J., and Y. L. Chen, 1999: A case study of nocturnal rain showers over the windward coastal region of the island of Hawaii. *Mon. Wea. Rev.*, **127**, 2674 - 2692.
- Nickerson, E. C., and Dias M. A., 1981: On the existence of atmospheric vortices downwind of Hawaii during the HAMEC project. *J. Appl. Meteor.*, **20**, 868–873.
- _____, 1979: On the numerical simulation of airflow and clouds over mountainous terrain. *Beitr. Phys. Atmos.* **52**, 161-177.
- Patzert, W. C., 1969: Eddies in Hawaiian waters. HIG Rep. No. HIG-69-8, Hawaii Institute of Geophysics, University of Hawaii, Honolulu, HI, 51pp.
- Rasmussen, R. M., and P. K. Smolarkiewicz, 1993: On the dynamics of Hawaiian cloud bands. Part III: local aspects, *J. Atmos. Sci.*, **50**, 1560-1572.
- _____, P. K. Smolarkiewicz and J. Warner, 1989: On the dynamics of Hawaiian cloud bands: comparison of model results with observations and island climatology. *J. Atmos. Sci.*, **46**, 1589-1608.

- Sato, H. H., W. Ikeda, R. Paeth, R. Smythe, and M. Takehiro, Jr., 1973: Soil survey of the island of Hawaii, State of Hawaii. United States Department of Agriculture, Soil Conservation Service, in cooperation with the University of Hawaii Agricultural Experiment Station.
- Schroeder, T., 1993: Climate controls. *Prevailing Trade Winds*, M. Sanderson, Ed., University of Hawaii Press, 12–36.
- _____, 1981: Characteristics of local winds in northwest Hawaii. *J. Appl. Meteor.*, **20**, 874–881.
- _____, B. J. Kilonsky, and B. N. Meisner, 1977: Diurnal variation in rainfall and cloudiness. UHMET Report 77-03, Department of Meteorology, University of Hawaii, 67 pp.
- Smith, R. B., and V. Grubisic, 1993: Aerial observation of Hawaii's wake, *J. Atmos. Sci.*, **50**, 3728–3750.
- Smolarkiewicz, P.K., R. M. Rasmussen, and T. L. Clark, 1988: On the dynamics of Hawaiian cloud bands: Island forcing, *J. Atmos. Sci.*, **45**, 1872–1905.
- Takahashi, T., 1986: Wind shear effects on water accumulation and rain duration in Hawaii warm clouds. *J. Meteor. Soc. Japan*. **64**, 575–584.
- _____, 1981: Warm rain study in Hawaii – Rain initiation. *J. Atmos. Sci.*, **38**, 347 – 369.
- Ueyoshi, K., 1990: A three-dimensional simulation of airflow and orographic rain over the island of Hawaii. Preprints, Fifth Con. On Mountain Meteorology. Boulder, CO., Amer. Meteor. Soc., J26-27.
- Wang, J.-J., R. M. Rauber, H. T. Ochs III, and R. E. Carbone, 2000: The effects of the island of Hawaii on offshore rainband evolution. *Mon. Wea. Rev.*, **128**, 1052–1069.

- _____, and Y.-L. Chen, 1998: A case study of trade-wind rainbands and their interaction with the island-induced airflow. *Mon. Wea. Rev.*, **126**, 409–423.
- _____, H.-M. H. Juang, K. Kodama, S. Businger, Y.-L. Chen, and J. Partain, 1998: Application of the NCEP Regional Spectral Model to improve mesoscale weather forecasts in Hawaii. *Wea. Forecasting*, **13**, 560–575.
- _____, and Y.-L. Chen, 1995: Characteristics of near surface winds and thermal profiles on the windward slopes of the Island of Hawaii. *Mon. Wea. Rev.*, **123**, 3481- 3501.
- Yang, Y., and Y.-L. Chen, 2003: Circulations and rainfall on the leeward side of the island of Hawaii during HaRP. *Mon. Wea. Rev.*, **131**, 2525-2542.
- Yeh, Hsi-Chyi, and Y.-L. Chen, 2003: Numerical simulations of the barrier jet over northwestern Taiwan during the Mei-Yu season. *Mon. Wea. Rev.*, **131**, 1396–1407.
- Zhang, D. – L., and R. A. Anthes, 1982: A high-resolution model of the planetary boundary layer sensitivity tests and comparisons with SESAME-79 data. *J. Appl. Meteor.*, **21**, 1594-1609.
- Zhang, Y., Y.-L. Chen, S.-Y. Hong, K. Kodama, and H.-M. H. Juang, 2005a: Validation of the coupled NCEP Mesoscale Spectral Model and an advanced Land Surface Model over the Hawaiian Islands. Part I: Summer trade wind conditions over Oahu and Heavy rainfall events. *Wea. Forecasting*. (Accepted with minor revisions).
- _____, _____, T. A. Schroeder, and K. Kodama, 2005b: Numerical simulations of the sea-breeze circulations over northwest Hawaii. *Wea. Forecasting*. (Accepted for publication).

Table captions

Table 1. Model sensitivity tests. Slab refers to the five-layer simple soil model. “NEW” refers to tests using new land use, soil type and vegetation fraction data (Zhang et al. 2005a). Spin-up “YES” refers to tests using improved initial soil moisture and soil temperature from the 24th hour simulation of the previous day after running the coupled MM5/LSM continuously for two months prior to the HaRP period.

Table 2. Error statistics of the simulated surface temperature deviations and mixing ratio (g kg^{-1}) at 50 PAM stations at 1400HST on 10 August 1990. The bias refers to simulation minus observations. The abs error refers to the mean absolute error.

Table 3. As in Table 2 but for 0500 HST.

Table 4. Observed and simulated ground temperatures ($^{\circ}\text{C}$) at 1400 HST on 9 August 1990 at PAM stations 15, 16 and 17.

TABLE 1. Model sensitivity tests. Slab refers to the five-layer simple soil model. “NEW” refers to tests using new land use, soil type and vegetation fraction data (Zhang et al. 2005a). Spin-up “YES” refers to tests using improved initial soil moisture and soil temperature from the 24th hour simulation of the previous day after running the coupled MM5/LSM continuously for two months prior to the HaRP period.

	Land sfc model	boundary scheme	Land use/Soil type	Spin-up
CTL	OSU-LSM	MRF	NEW	YES
TEST 1	Slab	Blackadar	MM5	NO
TEST 2	Slab	MRF	MM5	NO
TEST 3	OSU_LSM	MRF	MM5	NO
TEST 4	OSU_LSM	MRF	NEW	NO
TEST 5	OSU_LSM	ETA	NEW	YES

TABLE 2. Error statistics of the simulated surface temperature deviations and mixing ratio (g kg^{-1}) at 50 PAM stations at 1400HST on 10 August 1990. The bias refers to simulation minus observations. The abs error refers to the mean absolute error.

Tests	T bias mean	T RMSE	T abs error	Q bias mean	Q RMSE	Q abs error
CTL	-1.0	1.8	1.4	-0.7	1.8	1.2
Test 1	-3.1	3.6	3.2	-0.2	2.1	1.3
Test 2	-0.6	2.0	1.6	0.6	2.3	1.6
Test 3	-0.6	2.3	1.7	-0.7	2.0	1.2
Test 4	-1.3	2.0	1.6	-0.7	2.2	1.3
Test 5	-1.7	2.4	2.0	0.2	2.3	1.3

TABLE 3. As in Table 2 but for 0500 HST.

Tests	T bias mean	T RMSE	T abs error	Q bias mean	Q RMSE	Q abs error
CTL	0.3	1.2	1.0	-0.3	1.3	1.1
Test 1	0.8	1.6	1.3	1.2	1.8	1.5
Test 2	0.8	1.7	1.4	0.5	1.6	1.3
Test 3	1.1	1.9	1.6	1.1	1.9	1.5
Test 4	0.6	1.3	1.1	0.3	1.7	1.3
Test 5	-0.2	1.3	1.1	-0.9	1.9	1.3

TABLE 4. Observed and simulated ground temperatures (° C) at 1400 HST on 9 August 1990 at PAM stations 15, 16 and 17.

	Station 15	Station 16	Station 17
Observations	30.9	22.1	36.6
CTL	25.5	21.2	32.1
TEST3	25.1	20.3	24.3
TEST1	22.3	18.1	16.2

Figure captions

Figure 1. The island of Hawaii with PAM sites. Contours are for every 1000-m elevation.

Figure 2. The four domains employed in this study with resolutions of 81 km, 27 km, 9 km and 3 km, respectively.

Figure 3. The soil moisture volumetric content (m^3/m^3) after 60-day simulation prior to HaRP for (a) 10-cm soil depth layer and (b) 40-cm soil depth layer.

Figure 4. The daily average PAM winds during HaRP for (a) the simulation, and (b) observations. Pennants, full barbs, and half barbs represent 5, 1, and 0.5 m s^{-1} respectively (the same hereafter).

Figure 5. The mean (a) u -wind component, and (b) v -wind component (m s^{-1}) during HaRP for observations (solid lines) and simulation (dotted lines) at 50 PAM stations..

Figure 6. The mean wind speed (m s^{-1}) of July and August in 1990 at the 1000-hPa level from NCEP/NCAR reanalysis data. Contour interval of 0.5 m s^{-1} . The symbol “+” denotes the rawinsonde sites.

Figure 7. The mean upstream sounding for 22 days with an early morning aircraft sounding during HaRP. Wind vectors on the left (right) are the averaged winds from NCEP/NCAR reanalysis at 0200 HST (aircraft flight-level data in the early morning). The thick solid (dashed) lines show the mean temperature (dewpoint temperature) from NCEP/NCAR reanalysis. The thin solid (dashed) lines show the mean temperature (dewpoint temperature) from aircraft flight-level data.

Figure 8. (a) Composite surface winds over Hawaiian waters from 15-yr ship observations after Patzert (1969). (b) Mean simulated surface winds during HaRP.

Figure 9. The temperature deviations from the upstream environment at the same height for (a) the simulation and (b) observations at 1400 HST, and for (c) the simulation and (d) observations at 0500 HST. Star signs denote PAM station sites.

Figure 10. The RMSE of simulated surface temperature deviations ($^{\circ}$ C) at 50 PAM stations at (a) 1400 HST and (b) 0500 HST.

Figure 11. The mean surface relative humidity (%) during HaRP at 50 PAM stations for observations (solid lines) and simulation (dotted lines).

Figure 12. The average PAM winds during HaRP at 1400 HST for (a) observations, and (b) the simulation, and at 0200 HST for (c) observations, and (d) the simulation.

Figure 13. The average winds during HaRP throughout the diurnal cycle at stations 13, 15, 44, 10, and 4 on the windward lowlands west of Hilo for (a) observations, and (b) the simulation.

Figure 14. Winds about 150 m above sea level from 1706 HST to 1756 HST 1 August 1990 for (a) observations, and (b) simulation, and from 0609 HST to 0659 HST 2 August 1990 for (c) observations, and (d) simulation.

Figure 15. Mean wind profiles during HaRP at Hilo. MM5 14 and MM5 02 denote the simulated Hilo sounding at 1400 HST and 0200 HST, respectively. OBS 14 and OBS 02 denote mean wind profiles derived from Hilo rawinsonde data at 1400 HST and 0200 HST, respectively.

Figure 16. Time-pressure cross sections of potential temperature (K) at Hilo on August 10, 1990 with an interval of 1 K constructed from (a) rawinsonde data, and (b) simulation at a 3-h interval.

Figure 17. The simulated ground temperature with an interval of 4°C at 1400 HST for (a) TEST1, (b) TEST3, and (c) CTL. The model is initialized at 0200 HST on 9 August 1990.

Figure 18. The island-wide divergence (10^{-4}s^{-1}) computed from winds at 21 PAM stations along the coast of the island of Hawaii during the diurnal cycle for observations (solid line), CTL run (dotted line), and TEST3 (dashed line).

Figure 19. The vertical cross sections along the transect in Fig. 21f on the windward side: (a) simulated mean zonal wind speed with an interval of 1 m s^{-1} , and (b) mean virtual potential temperature with an interval of 1 K at 2000 HST during HaRP.

Figure 20. Same as Fig. 19 but for 0000 HST.

Figure 21. Simulated 4-h rainfall accumulation during HaRP. (a) 1900 – 2300 HST; (b) 2300 – 0300 HST; (c) 0300 – 0700 HST; (d) 0700 – 1100 HST; (e) 1100 – 1500 HST; (f) 1500 – 1900 HST.

Figure 22. Same as Fig. 19 but for 0400 HST.

Figure 23. Same as Fig. 19 but for 0800 HST.

Figure 24. Same as Fig. 19 but for 1400 HST.

Figure 25. The vertical cross sections along the transect in Fig. 21f at 0400 HST for (a) the simulated mean zonal wind speed deviations from the HaRP mean state with an interval of 0.5 m s^{-1} , (b) the simulated mean vertical velocity deviations from the HaRP mean state with an interval of 2.5 cm s^{-1} , (c) the wind vectors of simulated mean zonal wind speed deviations and mean vertical velocity deviations from the HaRP mean state, and (d) mean equivalent potential temperature with an interval of 1 K during HaRP.

Figure 26. Same as Fig. 25 but for 1400 HST.

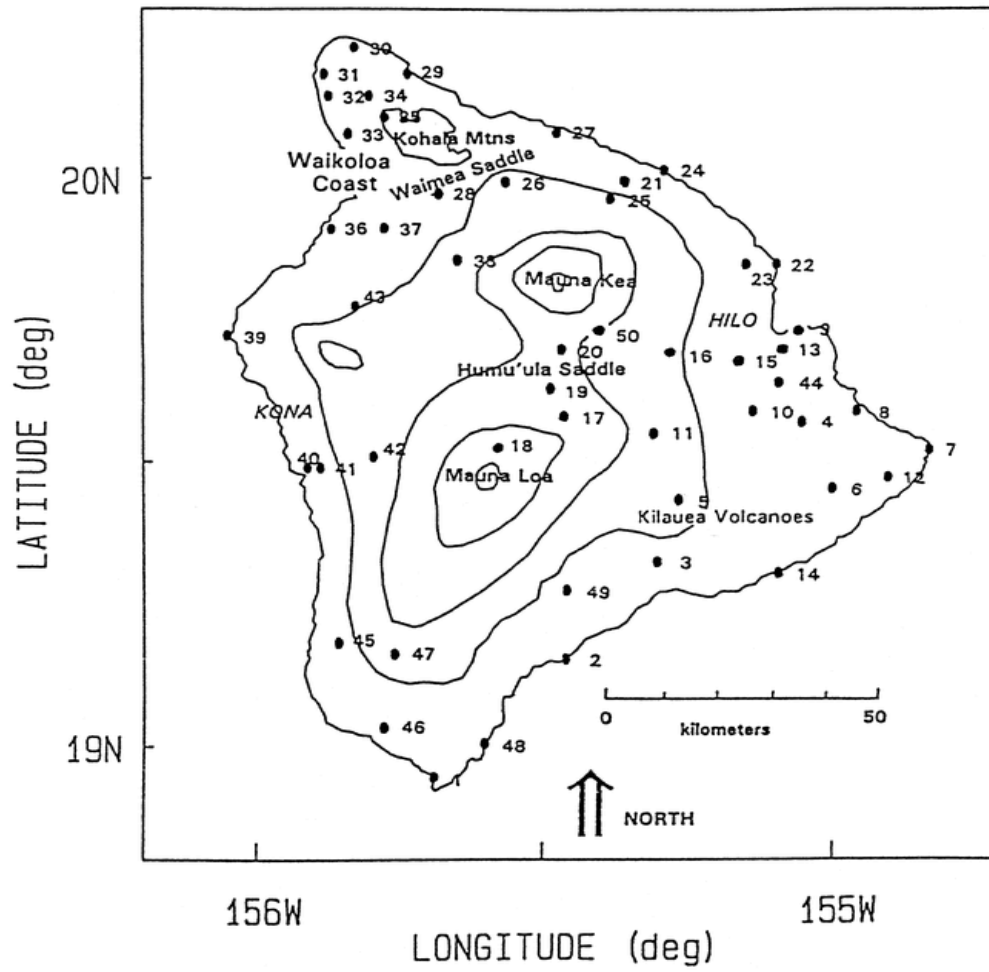


Figure 1. The island of Hawaii with PAM sites. Contours are for every 1000-m elevation.

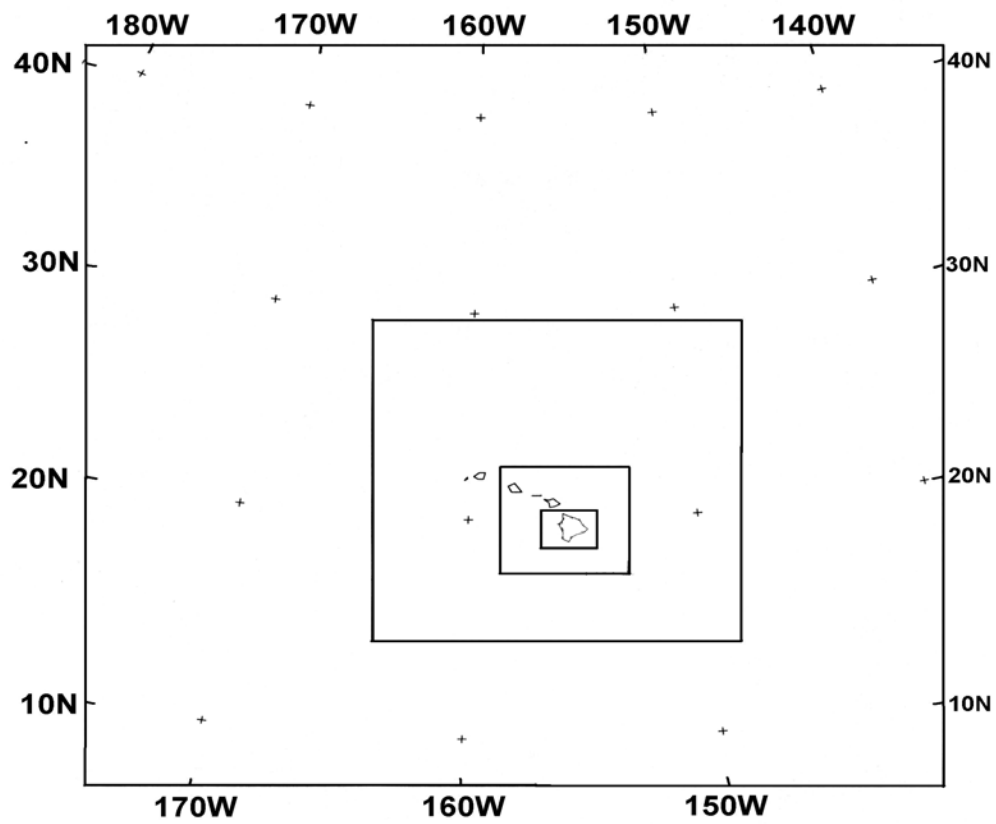


Figure 2. The four domains employed in this study with resolutions of 81 km, 27 km, 9 km and 3 km, respectively.

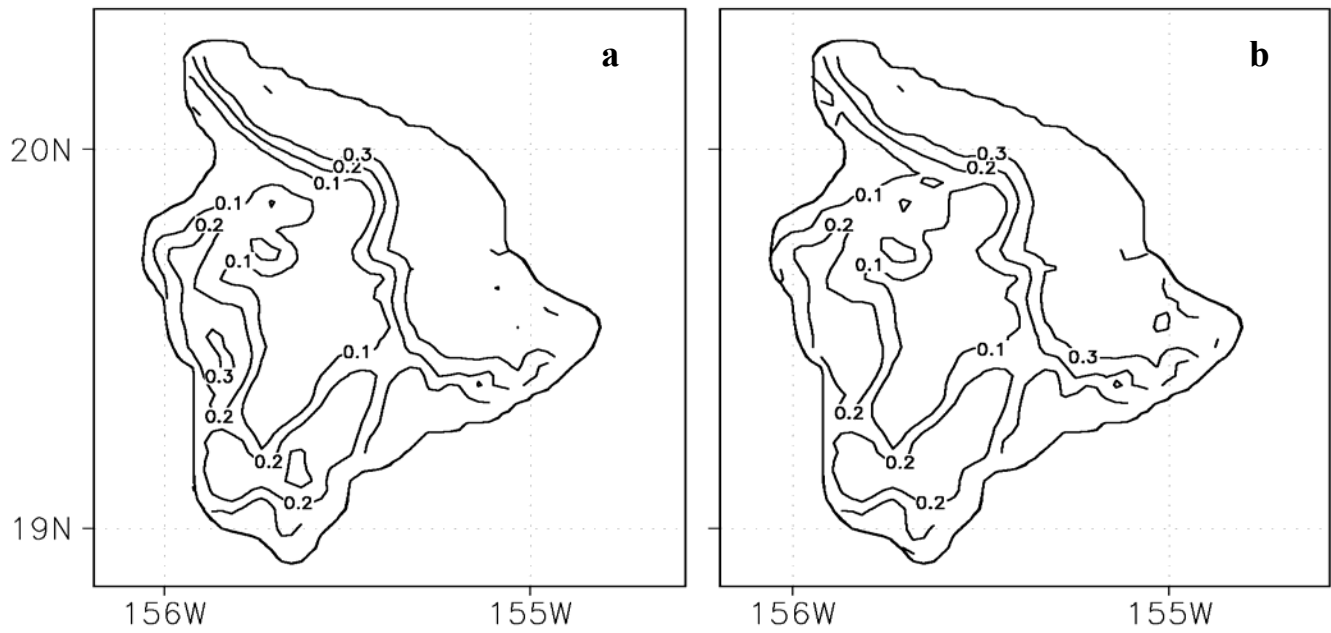


Figure 3. The soil moisture volumetric content (m^3/m^3) after 60-day simulation prior to HaRP for (a) 10-cm soil depth layer and (b) 40-cm soil depth layer.

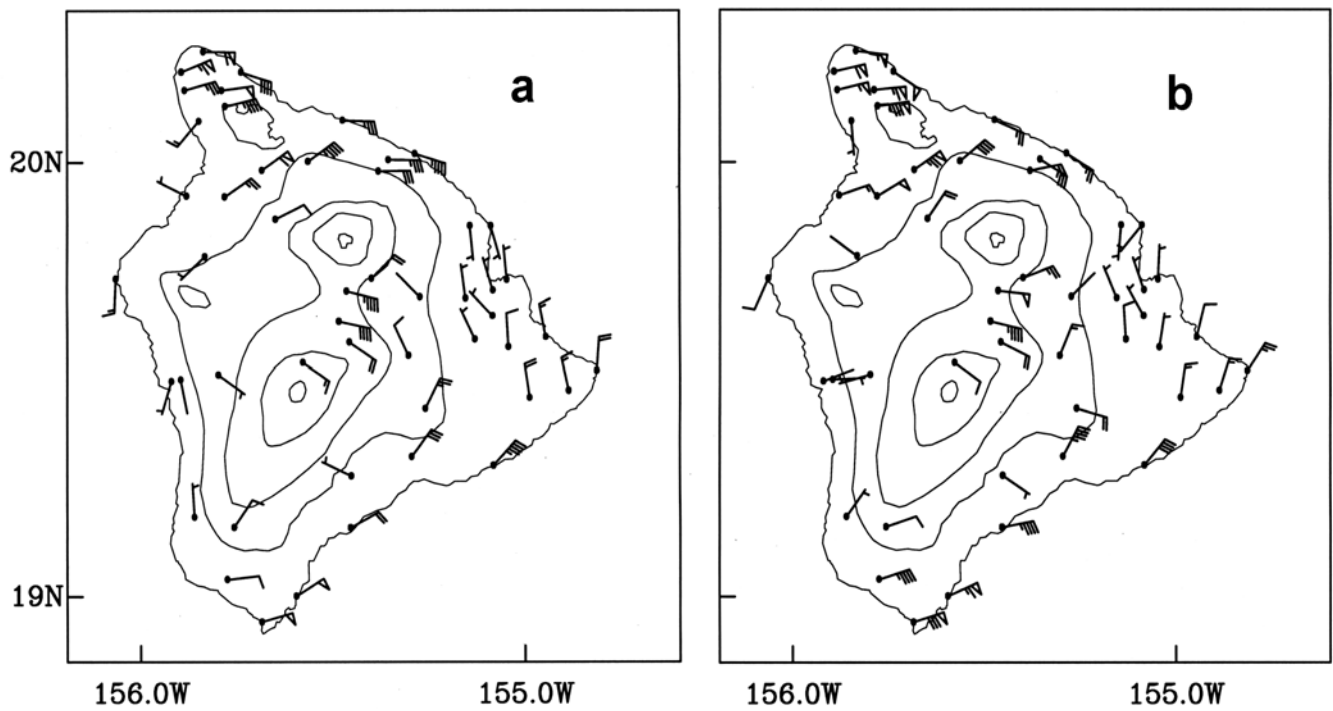


Figure 4. The daily average PAM winds during HaRP for (a) the simulation and (b) observations. Pennants, full barbs, and half barbs represent 5, 1, and 0.5 m s⁻¹ respectively (the same hereafter).

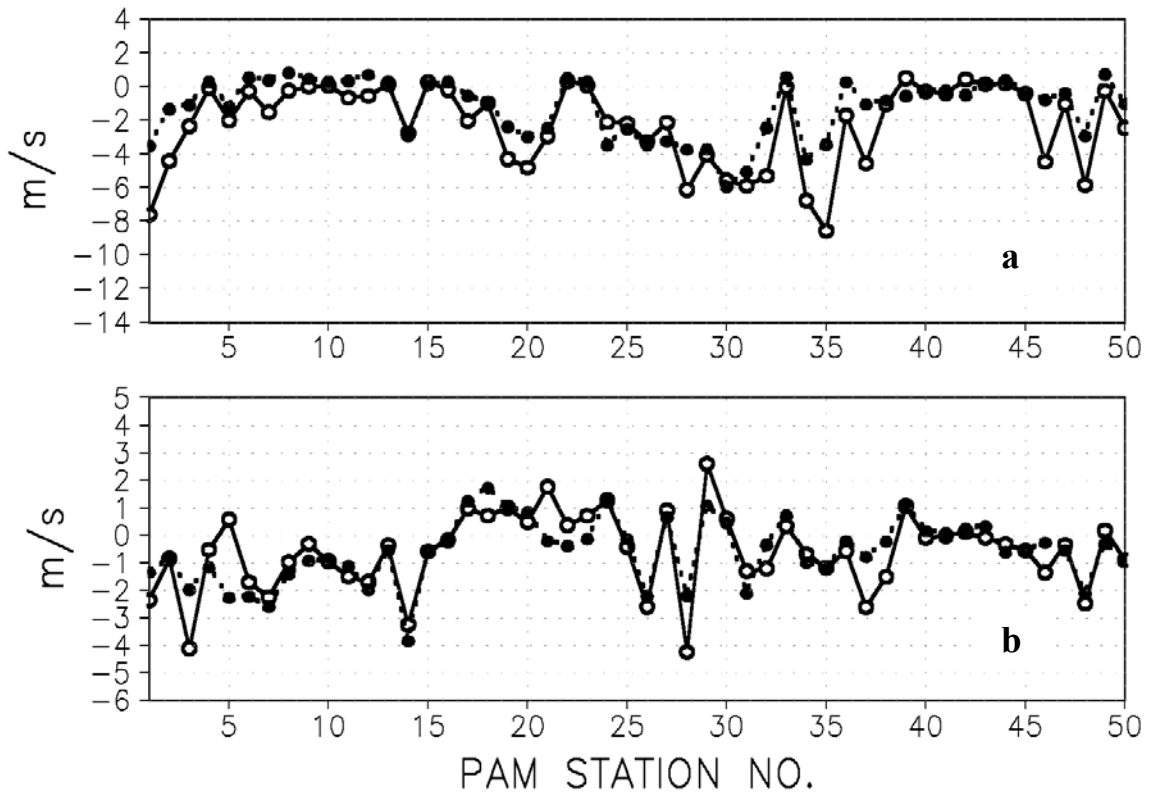


Figure 5. The mean in (a) u -wind component, and (b) v -wind component (m s^{-1}) during HaRP for observations (solid lines) and simulation (dotted lines) at 50 PAM stations.

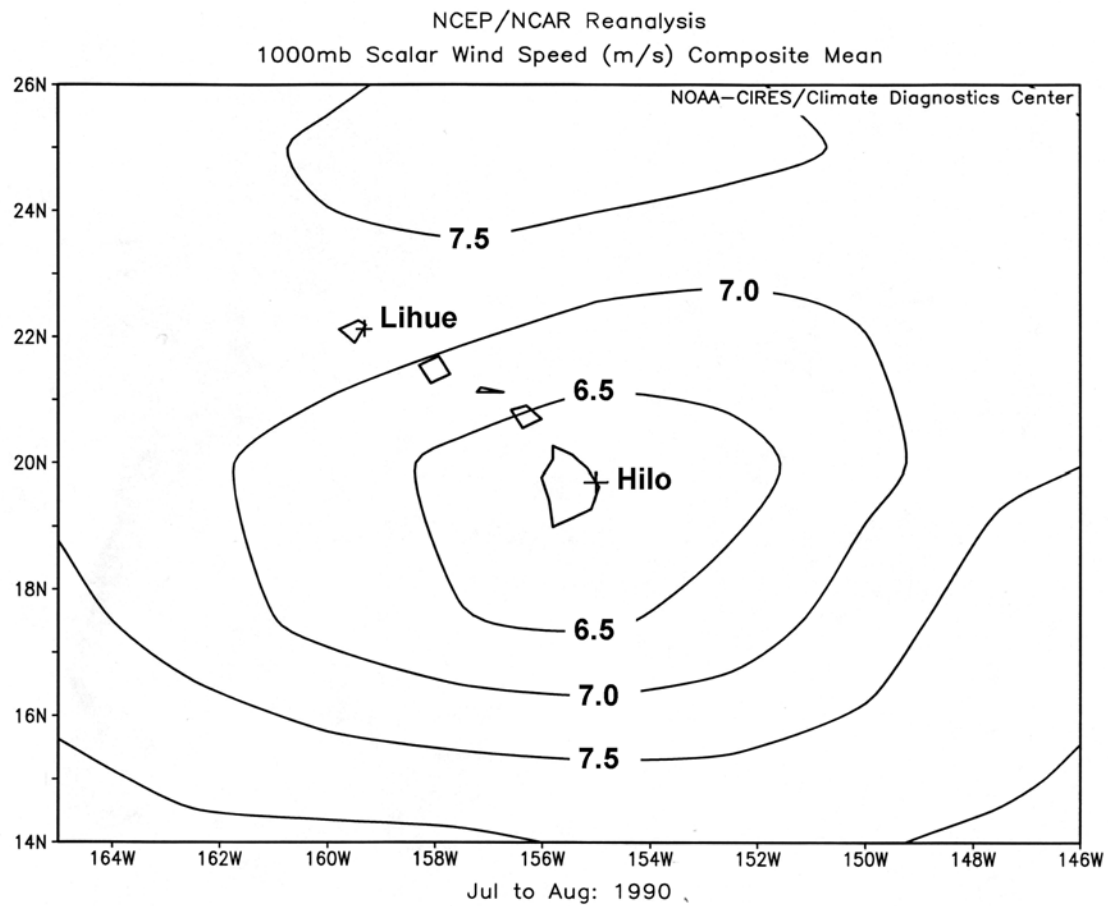


Figure 6. The mean wind speed (m s^{-1}) of July and August in 1990 at the 1000-hPa level from NCEP/NCAR reanalysis data. Contour interval of 0.5 m s^{-1} . The symbol “+” denotes the rawinsonde sites.

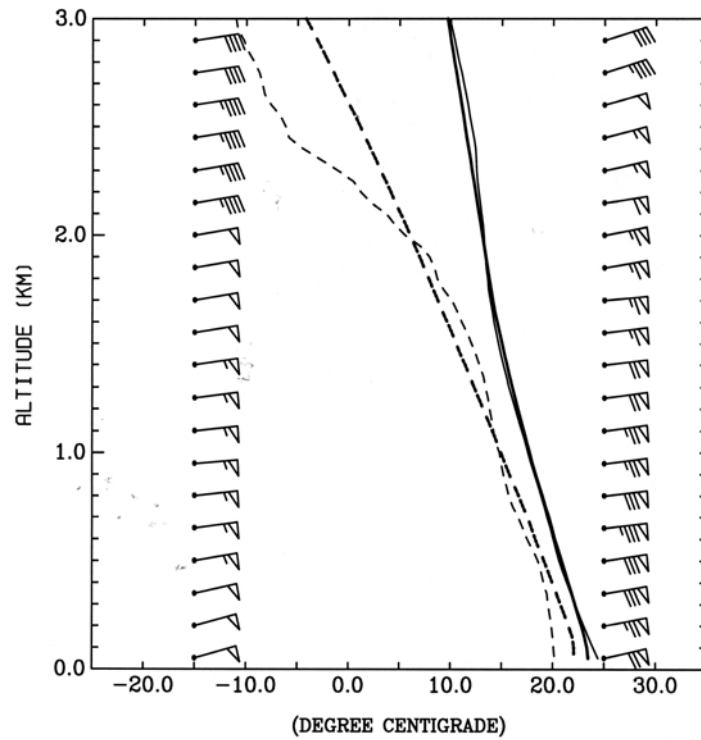


Figure 7. The mean upstream sounding for 22 days with an early morning aircraft sounding during HaRP. Wind vectors on the left (right) are the averaged winds from NECP/NCAR reanalysis at 0200 HST (aircraft flight-level data in the early morning). The thick solid (dashed) lines show the mean temperature (dewpoint temperature) from NCEP/NCAR reanalysis. The thin solid (dashed) lines show the mean temperature (dewpoint temperature) from aircraft flight-level data.

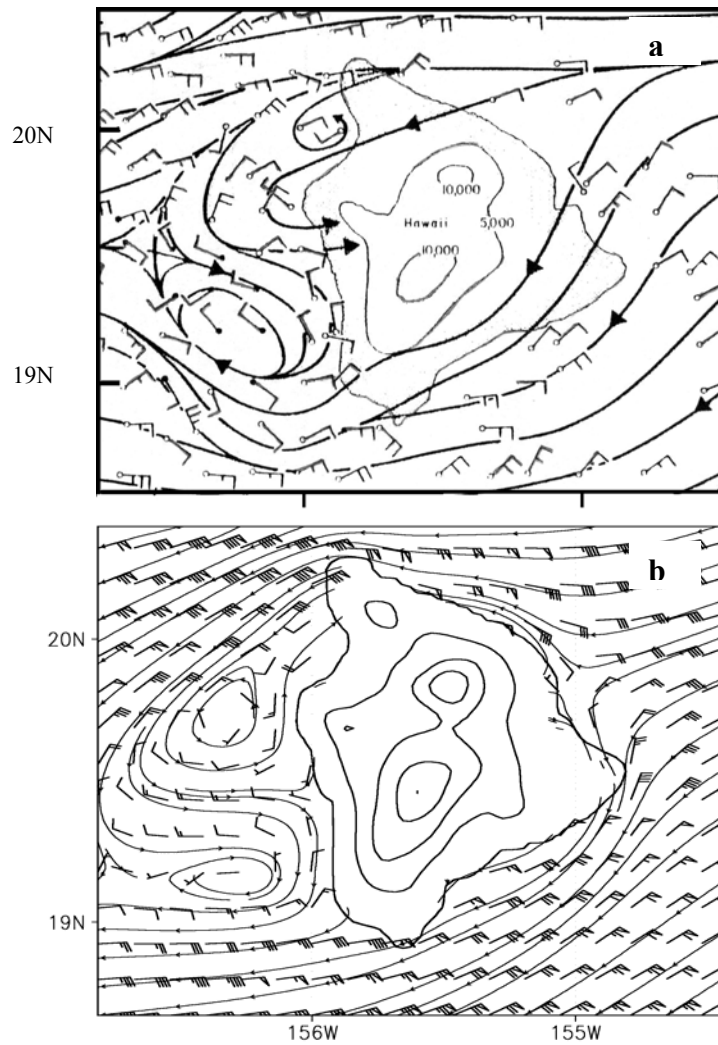


Figure 8. (a) Composite surface winds over Hawaiian waters from 15-yr ship observations after Patzert (1969). (b) Mean simulated surface winds during HaRP.

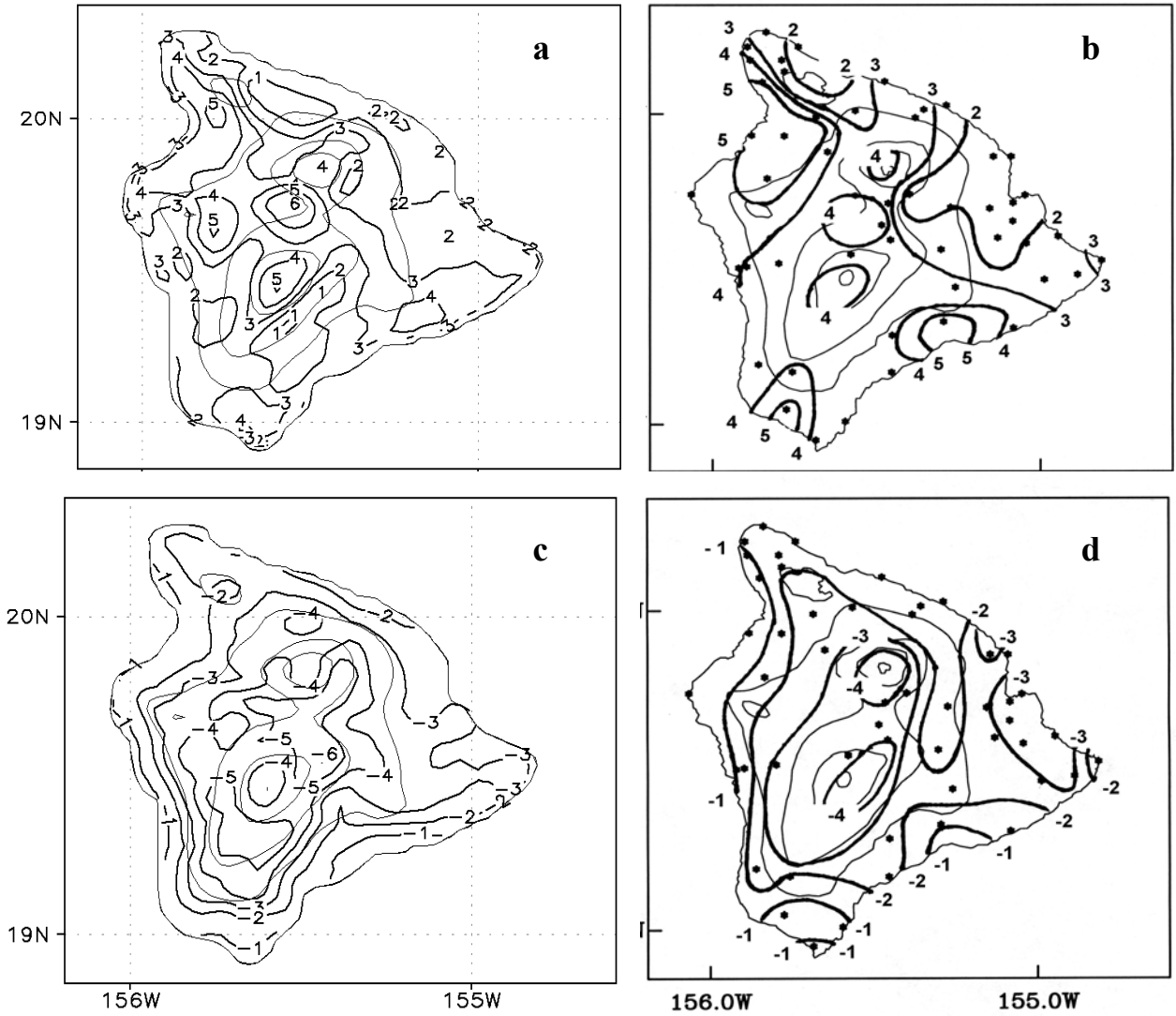


Figure 9. The temperature deviations from the upstream environment at the same height for (a) the simulation and (b) observations at 1400 HST, and for (c) the simulation and (d) observations at 0500 HST. Star signs denote PAM station sites.

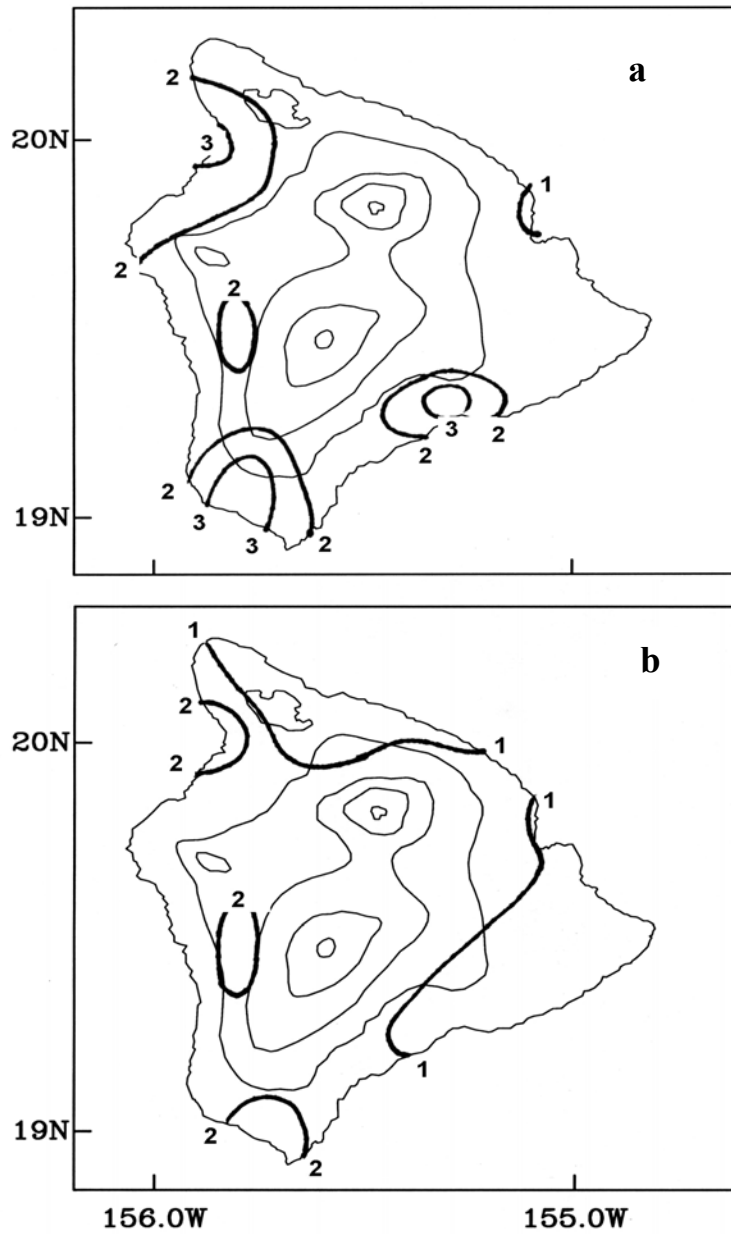


Figure 10. The RMSE of simulated surface temperature deviations at 50 PAM stations at (a) 1400 HST and (b) 0500 HST.

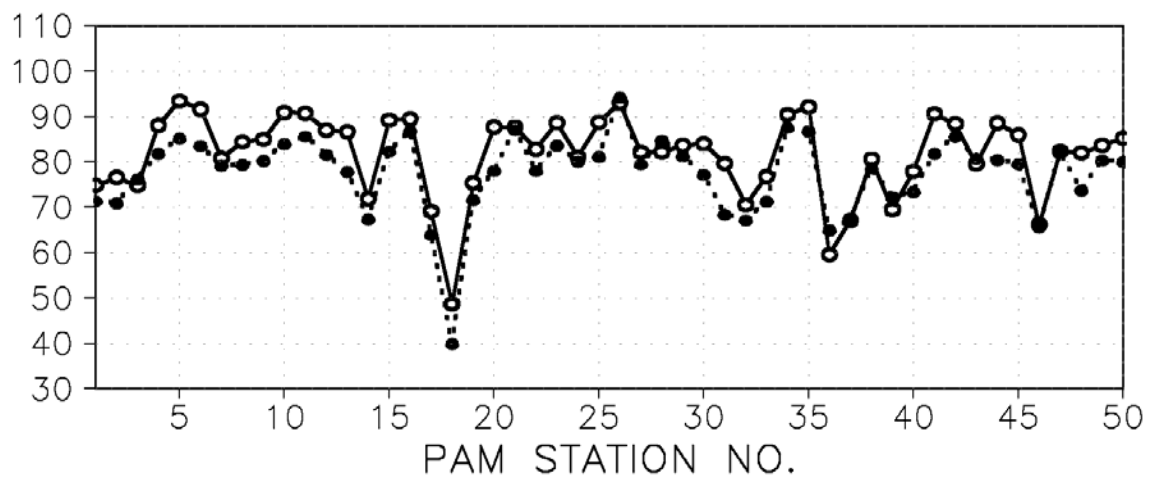


Figure 11. The mean surface relative humidity (%) during HaRP at 50 PAM stations for observations (solid lines) and simulation (dotted lines).

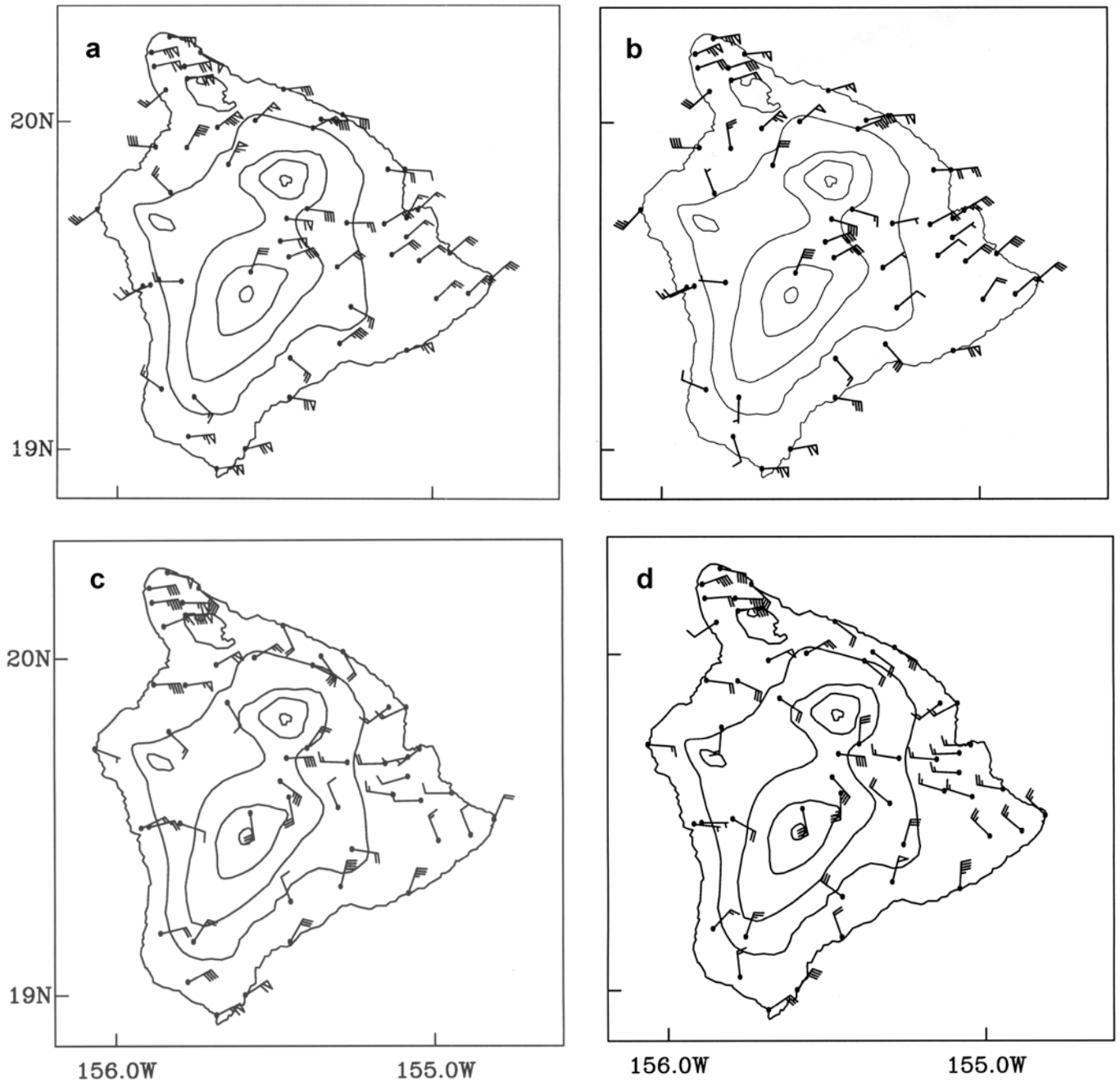


Figure 12. The average PAM winds during HaRP at 1400 HST for (a) observations and (b) the simulation, and at 0200 HST for (c) observations, and (d) the simulation.

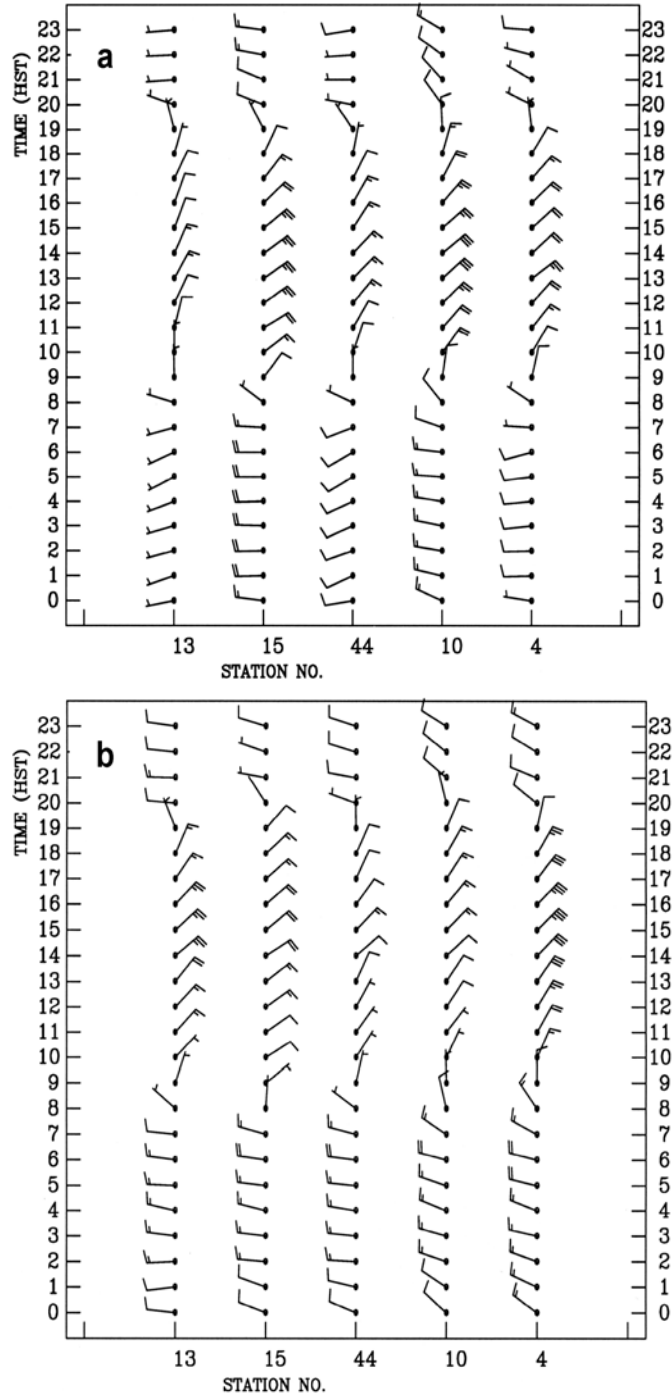


Figure 13. The average winds during HaRP throughout the diurnal cycle at stations 13, 15, 44, 10, and 4 on the windward lowlands west of Hilo for (a) observations, and (b) the simulation.

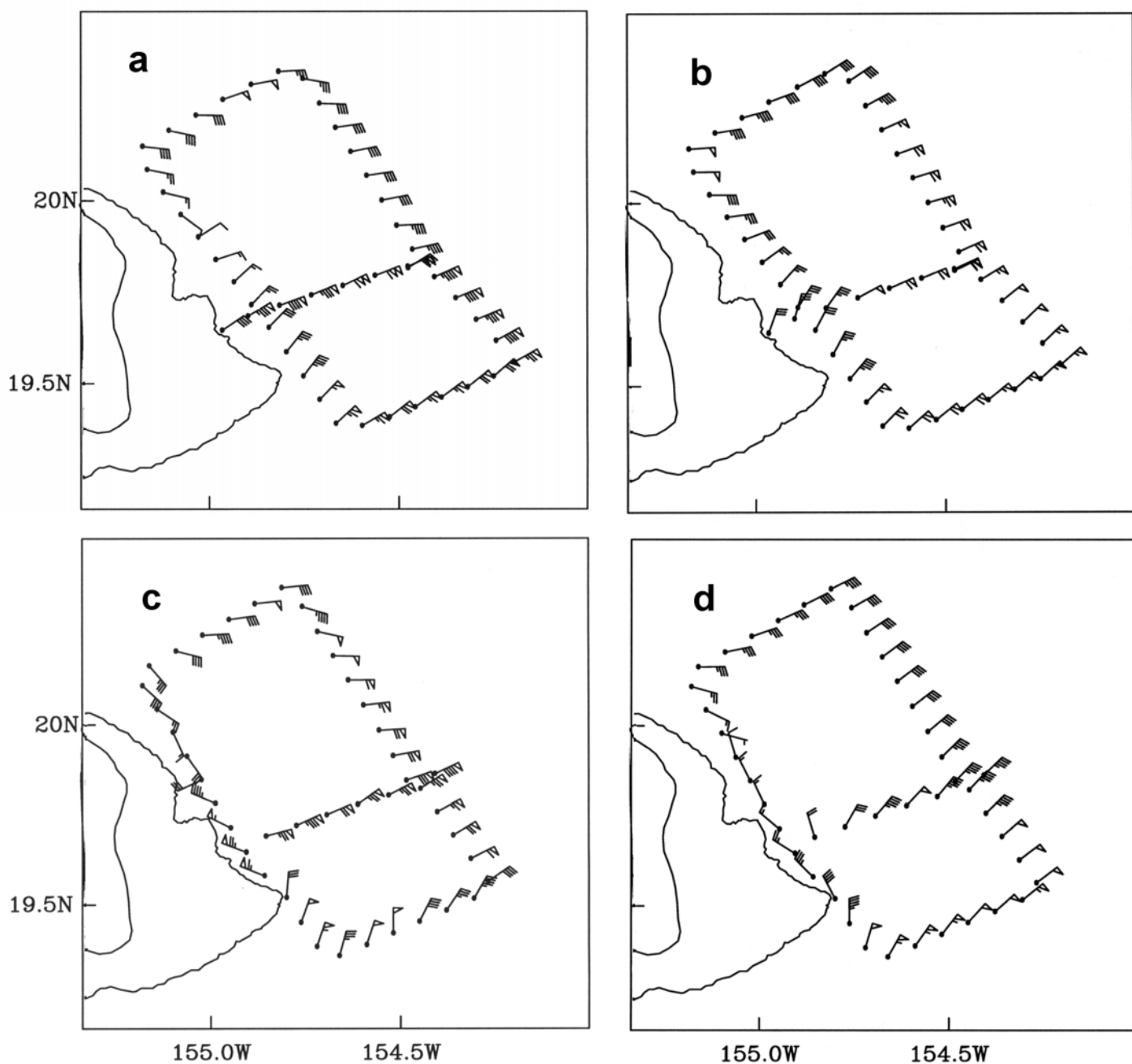


Figure 14. Winds about 150 m above sea level from 1706 HST to 1756 HST 1 August 1990 for (a) observations, and (b) simulation, and from 0609 HST to 0659 HST 2 August 1990 for (c) observations, and (d) simulation.

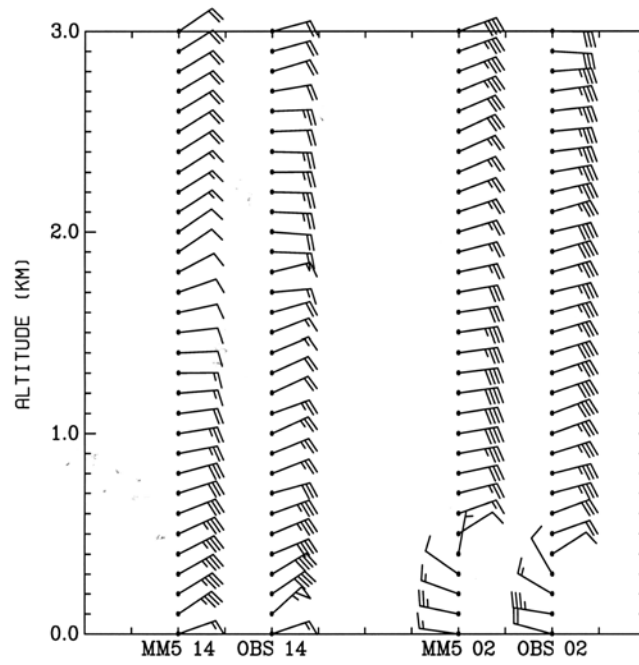


Figure 15. Mean wind profiles during HaRP at Hilo. MM5 14 and MM5 02 denote the simulated Hilo sounding at 1400 HST and 0200 HST, respectively. OBS 14 and OBS 02 denote mean wind profiles derived from Hilo rawinsonde data at 1400 HST and 0200 HST, respectively.

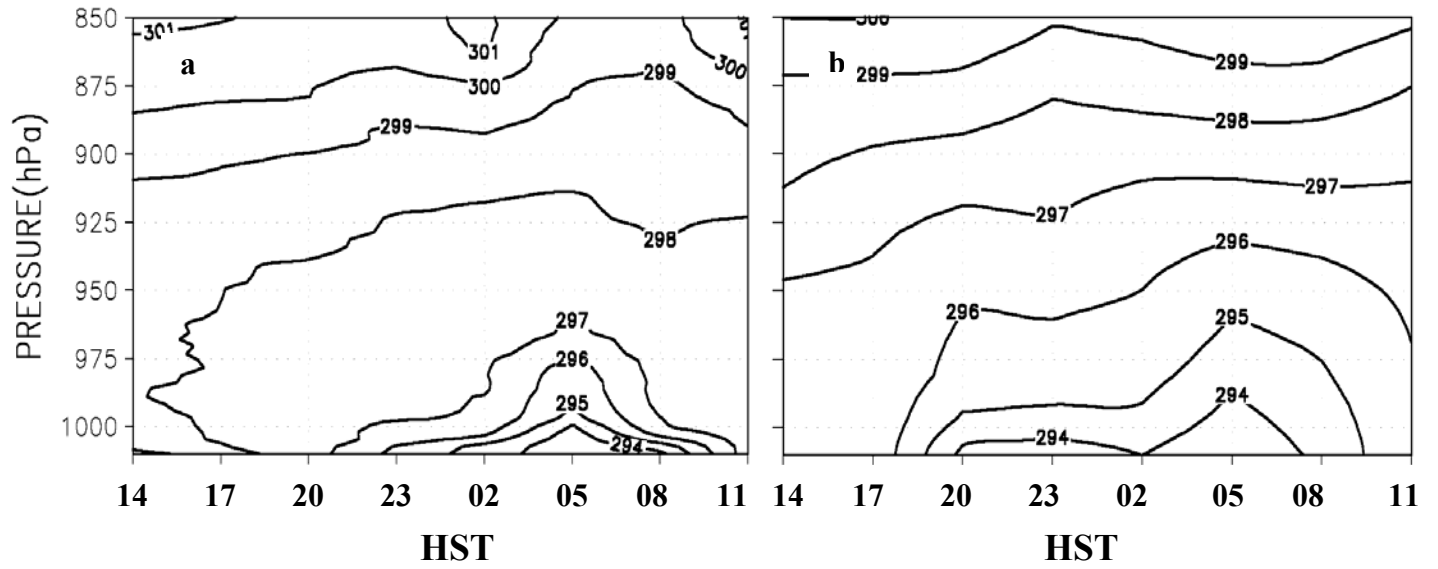


Figure 16. Time-pressure cross sections of potential temperature (K) at Hilo on August 10, 1990 with an interval of 1 K constructed from (a) rawinsonde data, and (b) simulation at a 3-h interval.

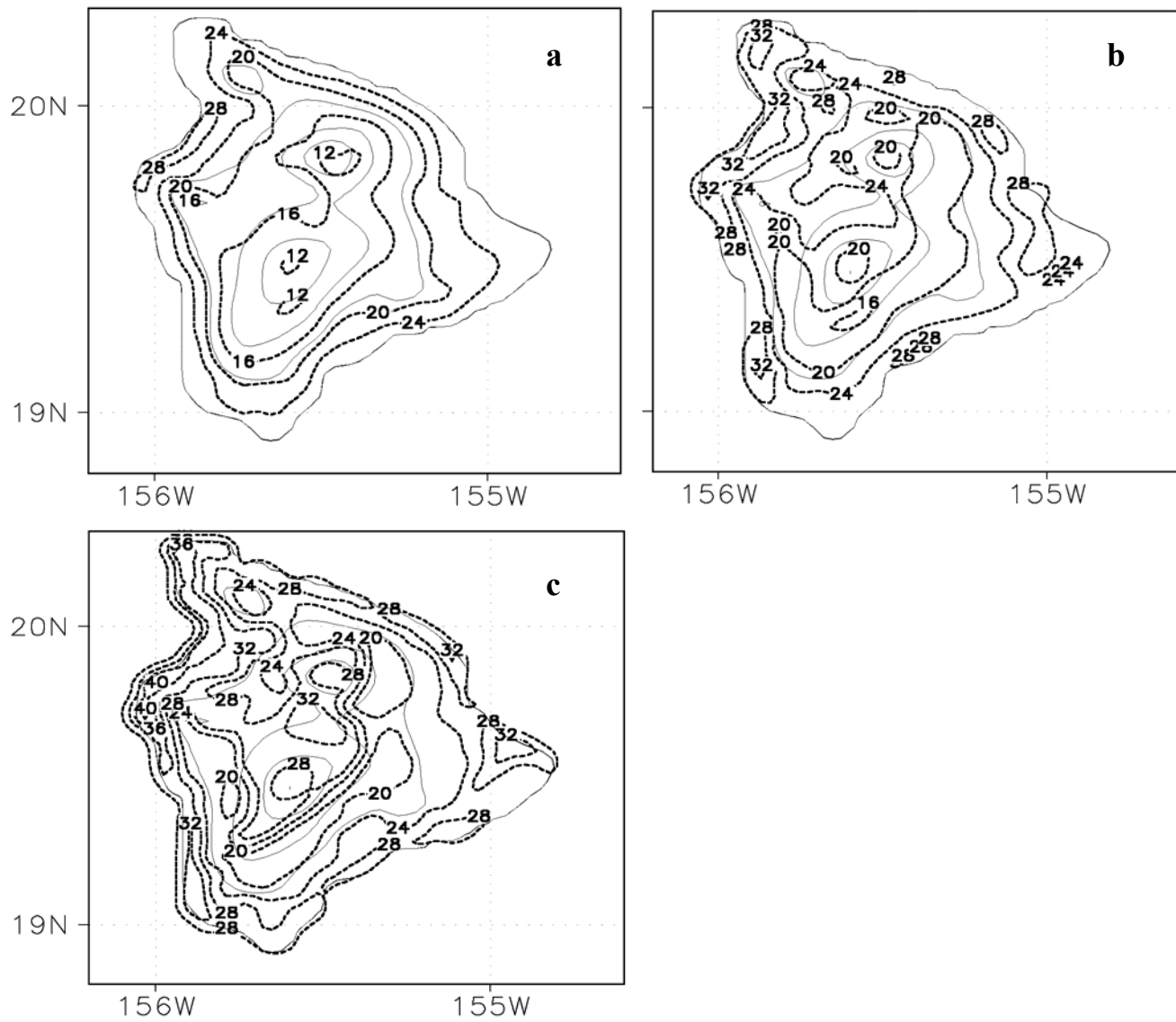


Figure 17. The simulated ground temperature with an interval of 4° C at 1400 HST for (a) TEST1, (b) TEST3, and (c) CTL. The model is initialized at 0200 HST on 9 August 1990.

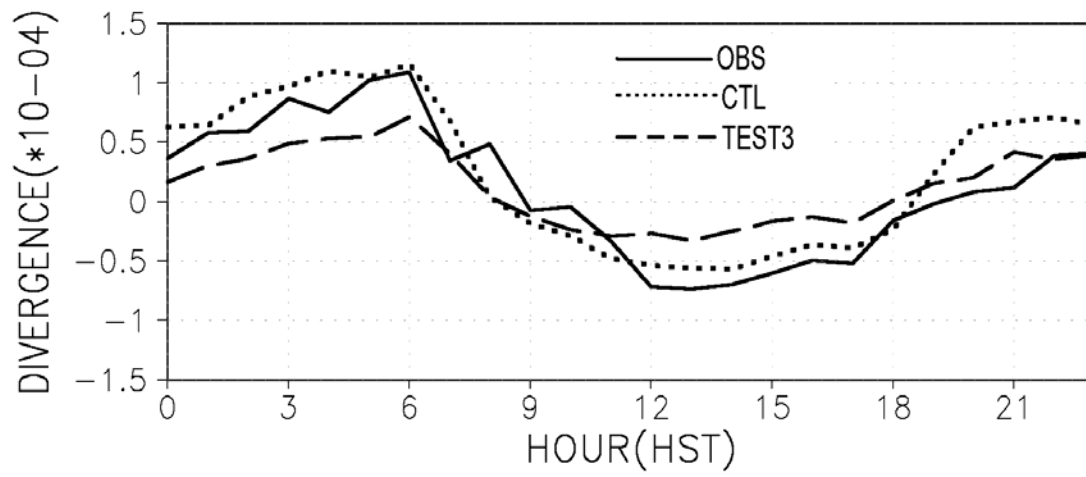


Figure 18. The island-wide divergence ($10^{-4} s^{-1}$) computed from winds at 21 PAM stations along the coast of the island of Hawaii during the diurnal cycle for observations (solid line), CTL run (dotted line), and TEST3 (dashed line).

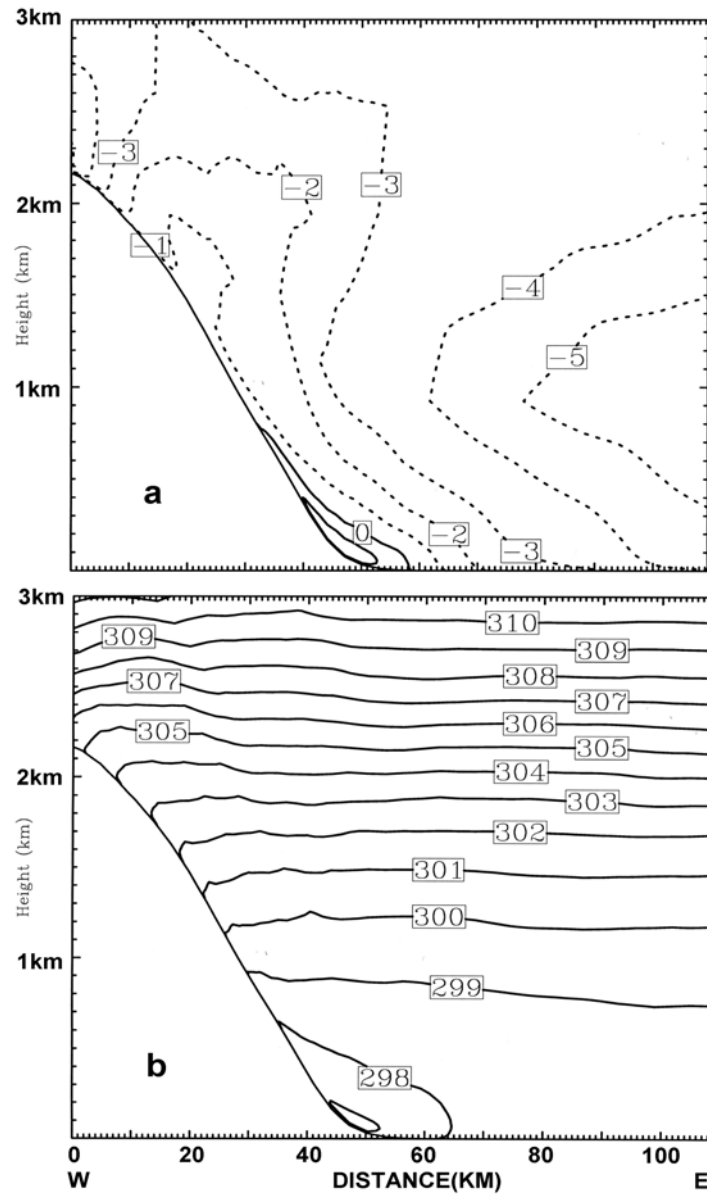


Figure 19. The vertical cross sections along the transect in Fig. 21f on the windward side:
 (a) simulated mean zonal wind speed with an interval of 1 m s^{-1} , and (b) mean
 virtual potential temperature with an interval of 1 K at 2000 HST during HaRP.

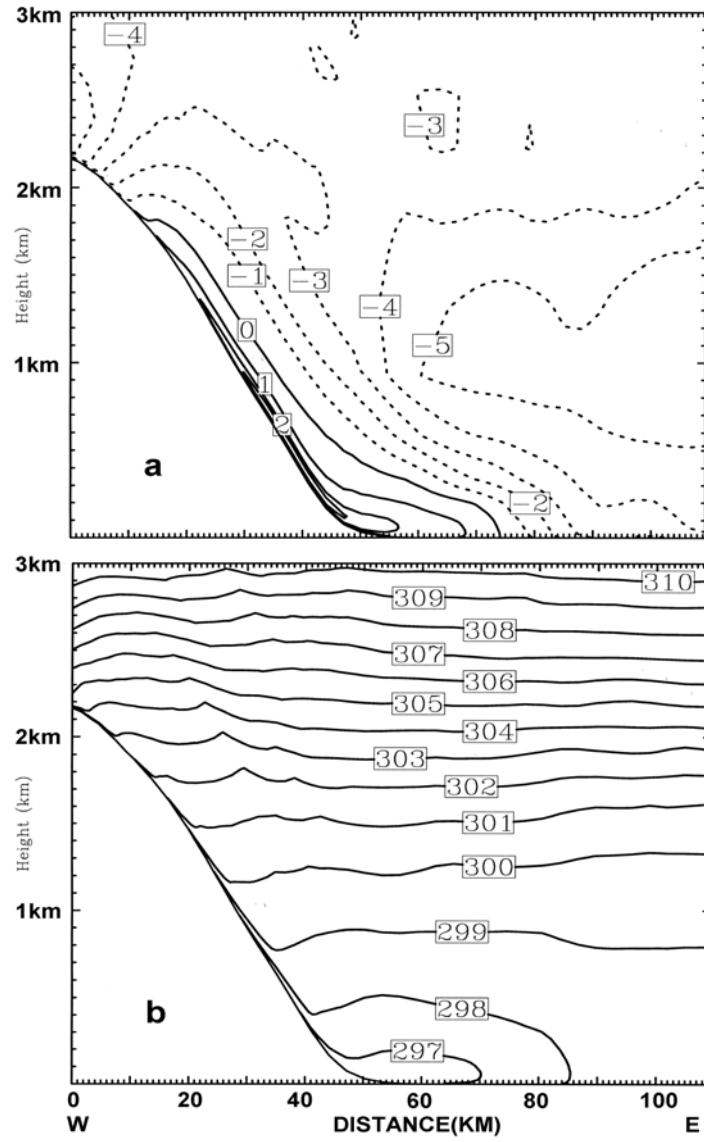


Figure 20. Same as Fig. 19 but for 0000 HST.

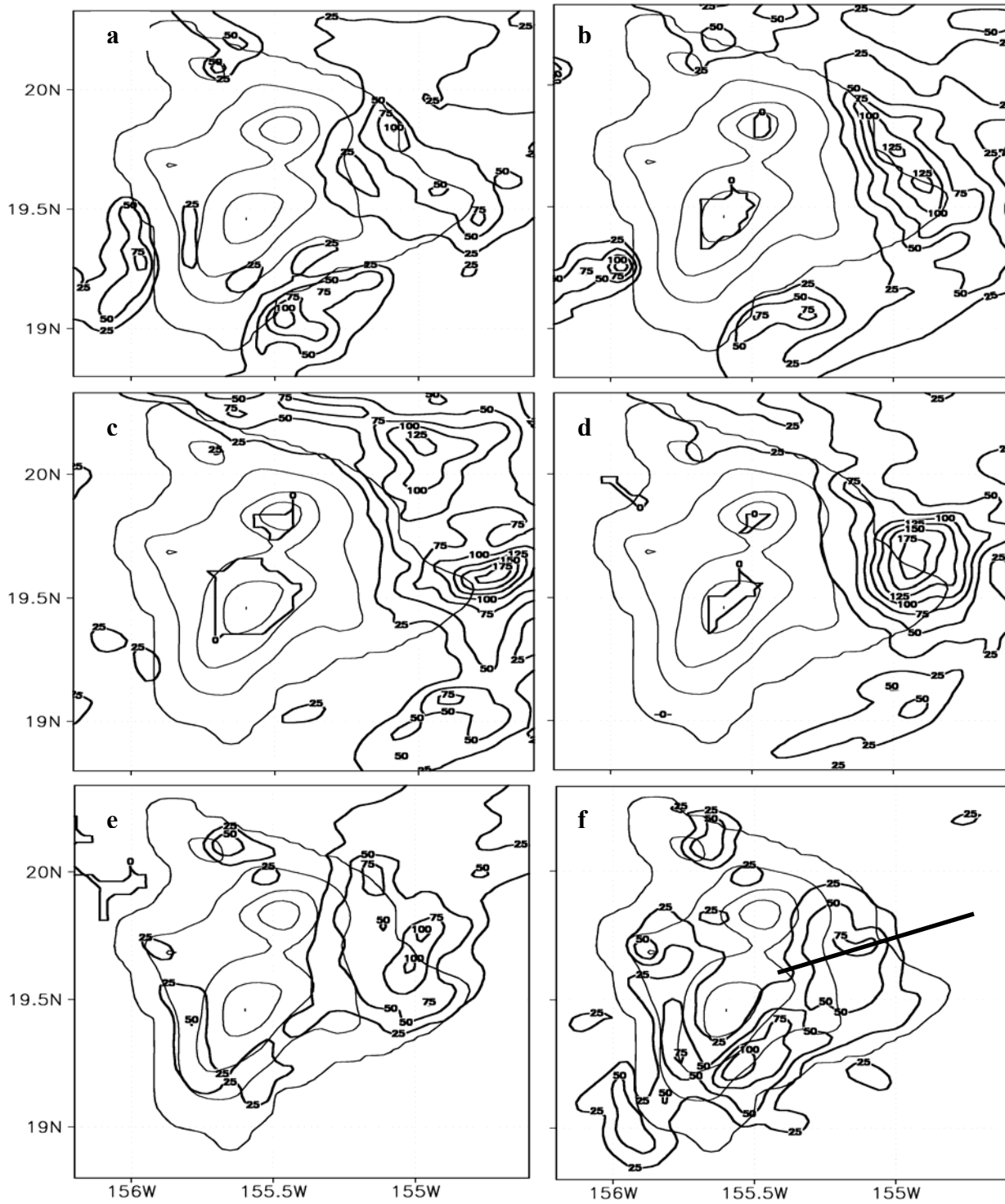


Figure 21. Simulated 4-h rainfall accumulation during HaRP. (a) 1900 – 2300 HST; (b) 2300 – 0300 HST; (c) 0300 – 0700 HST; (d) 0700 – 1100 HST; (e) 1100 – 1500 HST; (f) 1500 – 1900 HST.

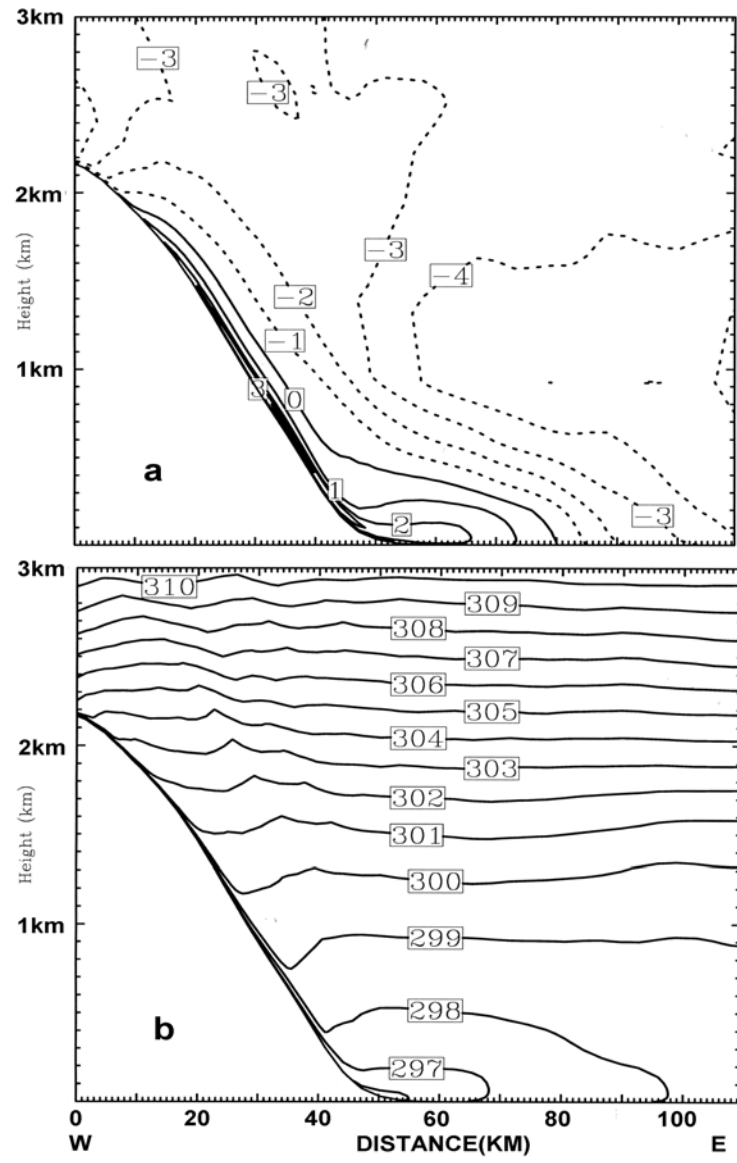


Figure 22. Same as Fig. 19 but for 0400 HST.

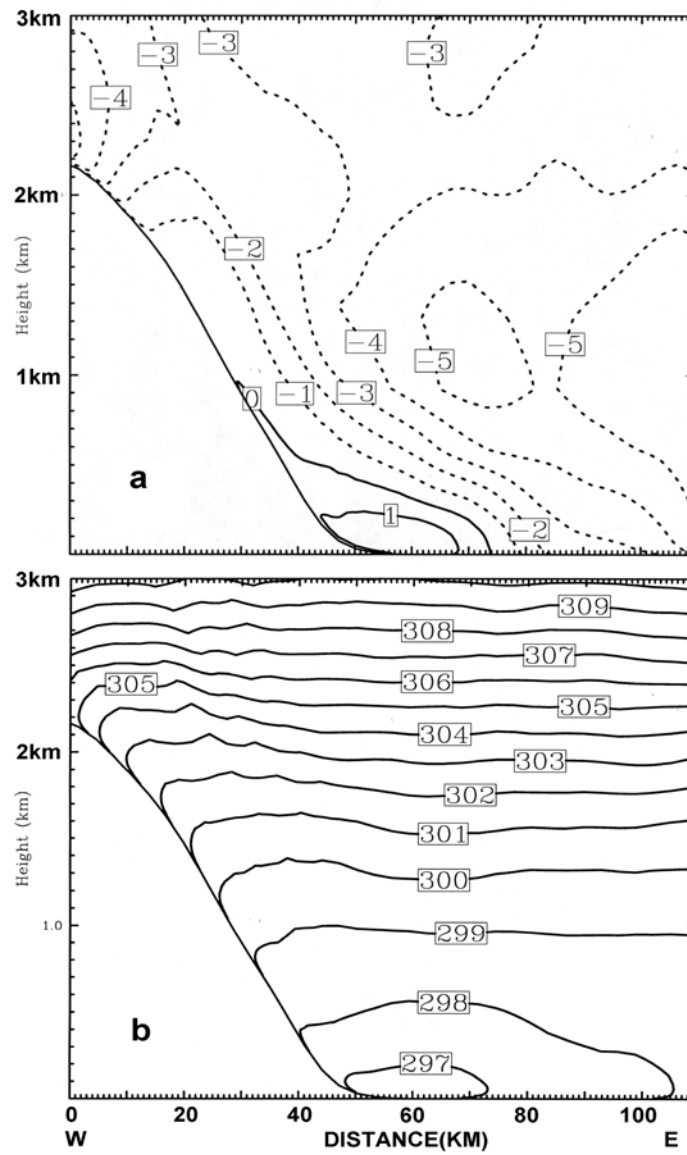


Figure 23. Same as Fig. 19 but for 0800 HST.

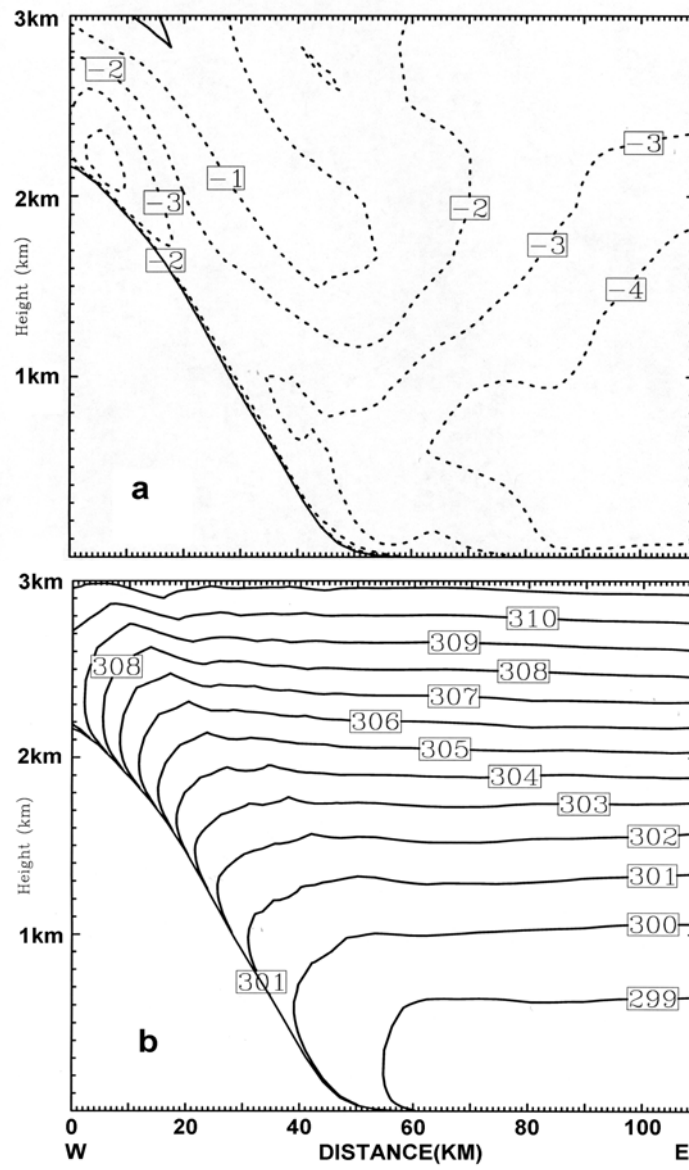


Figure 24. Same as Fig. 19 but for 1400 HST.

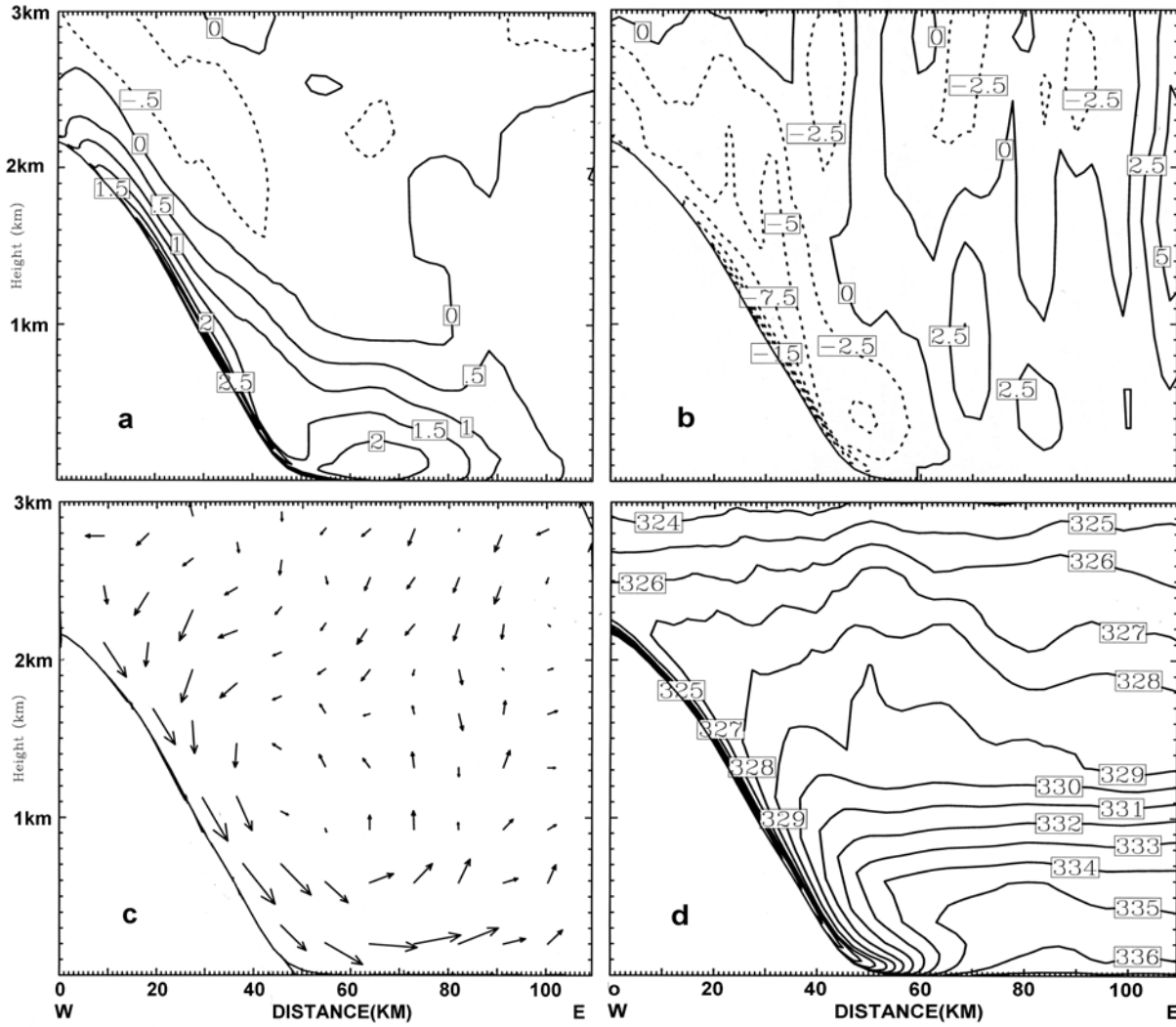


Figure 25. The vertical cross sections along the transect in Fig. 21f at 0400 HST for (a) the simulated mean zonal wind speed deviations from the HaRP mean state with an interval of 0.5 m s⁻¹, (b) the simulated mean vertical velocity deviations from the HaRP mean state with an interval of 2.5 cm s⁻¹, (c) the wind vectors of simulated mean zonal wind speed deviations and mean vertical velocity deviations from the HaRP mean state, and (d) mean equivalent potential temperature with an interval of 1 K during HaRP.

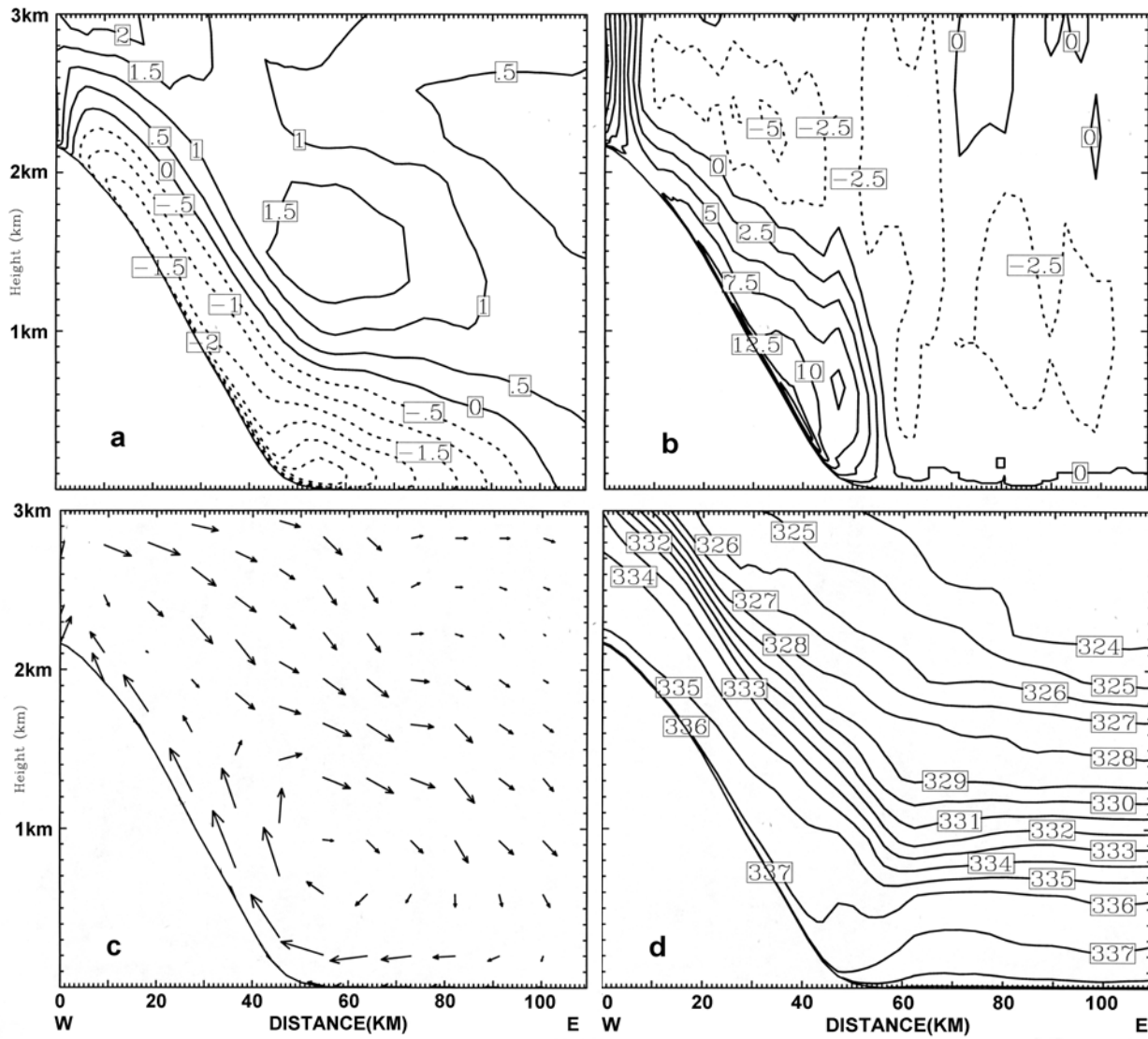


Figure 26. Same as Fig. 25 but for 1400 HST.